J. Fluid Mech. (2023), *vol*. 967, A40, doi:10.1017/jfm.2023.521

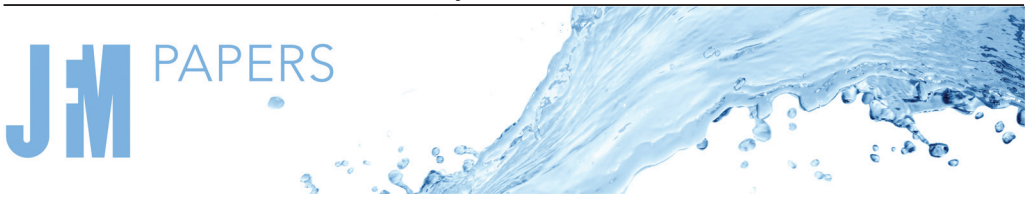

Large-scale motions in a turbulent natural convection boundary layer immersed in a stably stratified environment

K.R. Maryada[1],†, S.W. Armfield[2], P. Dhopade[1] and S.E. Norris[1]

[1]Department of Mechanical and Mechatronics Engineering, The University of Auckland, Auckland 1010, New Zealand

[2]School of Aerospace, Mechanical and Mechatronic Engineering, The University of Sydney, New South Wales 2006, Australia

(Received 23 January 2023; revised 5 May 2023; accepted 19 June 2023)

This study investigates the coherence of turbulent fluctuations in a turbulent vertical natural convection boundary layer immersed in a stably stratified medium (turbulent buoyancy layer). A turbulent buoyancy layer of a fluid having a Prandtl number of 0.71 at a Reynolds number of 800 is numerically simulated using direct numerical simulation. The two-point correlations reveal that the streamwise velocity fluctuations are coherent over large streamwise distances, with the length scale of the streamwise coherence being greater than the boundary layer thickness. This is due to large-scale motions (LSMs), similar to the LSMs observed in canonical wall-bounded turbulence despite the stark differences in flow dynamics. Both high-speed (positive) and low-speed (negative) streamwise velocity fluctuations form LSMs, with their streamwise length scales increasing with increasing wall-normal distance. High-speed LSMs are composed of upwash flow with high temperatures, while low-speed LSMs are composed of downwash flow with low temperatures. Both high-speed and low-speed LSMs meander appreciably in the streamwise direction, with the degree of meandering being correlated with the sign of the spanwise velocity fluctuations. The LSMs exhibit coherence across significant wall-normal distances and contribute significantly to the turbulence production in the outer layer. Examining the one-dimensional energy spectra of the turbulent buoyancy layer shows that the LSMs are the dominant energy-containing motions, implying that the length scale of the energy-containing range is of the order of boundary layer thickness. Notably, wall-normal velocity, spanwise velocity and buoyancy fluctuations do not form LSMs with streamwise length scales comparable to streamwise velocity fluctuations.

Key words: buoyant boundary layers, turbulent convection, boundary layer structure

† Email address for correspondence: kmar699@aucklanduni.ac.nz

1. Introduction

Coherent structures in wall-bounded turbulence play a crucial role in turbulence research due to their significant turbulent momentum and heat transport. Consequently, they have been a focus of numerous experimental, theoretical and numerical studies spanning several decades (the reader is referred to Robinson (1991), Adrian (2007), Smits, McKeon & Marusic (2011), Marusic & Adrian (2012) and Jiménez (2018) for reviews on the subject of coherent structures in wall-bounded turbulence).

Steadily, through the years, with the help of experiments and direct numerical simulations (DNSs), there has been ever-growing evidence of superstructures, large-scale motions and very-large-scale motions in turbulent channel, pipe and boundary layer flows (e.g. Kim & Adrian 1999; Marusic 2001; Ganapathisubramani *et al.* 2005; Hutchins & Marusic 2007; Dennis & Nickels 2011; Baltzer, Adrian & Wu 2013; Hwang *et al.* 2016; Lee 2017). The term superstructures is often associated with turbulent boundary layers, and these correspond to motions whose dimensions are significantly greater than the boundary layer thickness δ_{TBL}. In turbulent boundary layers, these motions were found to have streamwise wavelengths of the order of $6\delta_{TBL}$ (Hutchins & Marusic 2007; Lee & Sung 2011). Large-scale motions and very-large-scale motions, on the other hand, are usually associated with turbulent channel and pipe flows. In this context, large-scale motions have streamwise lengths greater than the outer length scale h (half-channel width or pipe radius) but less than $3h$. Very-large-scale motions refer to motions whose streamwise length scales are greater than $3h$ (Lee *et al.* 2014; Lee, Ahn & Sung 2015; Hwang *et al.* 2016). Turbulent boundary layers, channel flows and pipe flows are termed canonical wall-bounded turbulence and superstructures, large-scale and very-large-scale motions are collectively termed large-scale motions (LSMs) from hereon. Despite significant quantitative differences, the LSMs are qualitatively similar across turbulent channel, pipe and boundary layer flows (Monty *et al.* 2007; Lee & Sung 2013; Lee *et al.* 2015). The LSMs have been shown to carry significant portions of the turbulent kinetic energy (TKE) and Reynolds shear stress, with their energy content increasing with increasing Reynolds numbers. It should be noted that the LSMs do not directly correspond to the general integral-scale motions that are present in turbulent flows.

Compared with canonical wall-bounded turbulence, the turbulent structure of natural convection boundary layers (NCBLs) is poorly understood. The present study concerns a turbulent NCBL immersed in a stably stratified environment. However, as NCBLs immersed in stably stratified media share many qualitative similarities with their unstratified counterparts, the literature concerning the turbulent structure of unstratified NCBLs is briefly reviewed here.

Most early experiments and numerical simulations concerning turbulent NCBLs dealt with the mean streamwise velocity field, mean temperature field and one-point statistics (Gebhart 1973). Using experiments, the mean streamwise velocity profiles, temperature profiles and heat transfer correlations at several Grashof numbers were reported by Eckert & Jackson (1950), Cheesewright (1968) and Vliet & Liu (1969). Vliet & Liu (1969) also argued that the mean profiles of velocity and temperature fields in the outer layer could be approximated using universal power-law relationships.

There have been several attempts to understand the spatio-temporal structure of unstratified vertical NCBLs. Several numerical simulations and experiments were undertaken to uncover the flow structures in transitional unstratified NCBLs. It was shown that the NCBLs undergoing K-type and H-type transitions exhibit two-dimensional streamwise waves at the start of the transition. The Λ-structures dominate the flow field during the later stages of transition, and these flow structures are qualitatively similar to

the Λ-structures of transitional zero pressure gradient turbulent boundary layers despite differences in the flow dynamics (Zhao, Lei & Patterson 2017, 2019). For a Prandtl number Pr of 7.0, during the transition process, buoyancy contributes significantly towards TKE production when compared with the Reynolds shear stress (Zhao *et al.* 2017). Experiments and numerical simulations also revealed that secondary mean flows in the form of longitudinal rolls also populate the NCBL during the transition process (Jaluria & Gebhart 1974; Zhao, Lei & Patterson 2016; Zhao *et al.* 2017). A three-layer longitudinal system was observed during the K-type transition, while a two-layer longitudinal system was observed during the H-type transition (Zhao *et al.* 2017).

Regarding turbulent NCBLs, Fujii (1959), based on flow visualisation, argued the presence of a 'vortex-street-like instability' in the outer layer. Tsuji & Nagano (1988*a*), apart from making detailed investigations into the mean profiles and one-point statistics, investigated the boundary layer structure close to the wall. The authors found that a viscous sublayer analogous to the linearly varying viscous sublayer in canonical wall-bounded turbulence is absent close to the wall. This was also confirmed in the high Grashof number DNS study of Ke *et al.* (2020), where this behaviour was attributed to buoyancy effects. Tsuji & Nagano (1988*b*) made accurate measurements of Reynolds shear stress and turbulent heat flux and confirmed the observations of Tsuji & Nagano (1988*a*) regarding the unique turbulent structure of NCBLs. Nakao, Hattori & Suto (2017) investigated the turbulent structure of a spatially developing vertical NCBL using large-eddy simulation (LES) and showed that the outer layer was more turbulent than the inner layer at the Grashof numbers investigated. Using quadrant analysis (Wallace 2016) and flow visualisation, Hattori *et al.* (2006) and Nakao *et al.* (2017) showed that the turbulent structure was significantly different from what was observed in turbulent boundary layers. In this context, the inner layer is defined as the region between the wall and the maximum velocity location. The outer layer is the region between the maximum velocity location and the edge of the boundary layer (Tsuji & Nagano 1988*b*; Hattori *et al.* 2006; Nakao *et al.* 2017).

Experiments concerning turbulent vertical NCBLs by Lock & Trotter (1968), Cheesewright & Doan (1978), Kitamura *et al.* (1985) and Hattori *et al.* (2006) revealed that the turbulent length scales are significant and that the large-scale eddies in NCBLs are essential for turbulent momentum and heat transport. The results from the DNS studies of Abramov, Smirnov & Goryachev (2014) and Ke *et al.* (2021) hinted at large-scale velocity structures in the outer layer of a temporally evolving unstratified NCBL. Large-scale structures were also observed in turbulent differentially heated channels (Versteegh & Nieuwstadt 1998; Ng *et al.* 2017; Kim, Ahn & Choi 2021). Although large-scale eddies have been hinted at in several studies, there has yet to be a study that thoroughly investigates the statistical properties of these large-scale eddies.

The experiments of Tsuji, Nagano & Tagawa (1992) revealed LSMs in the instantaneous temperature fields; however, the space–time correlations did not suggest the presence of streaks or bursts. This led the authors to conclude that the spanwise periodic streaky structures observed in turbulent boundary layers were absent in the temperature field of NCBLs. Abedin, Tsuji & Lee (2012) also argued against well-ordered fluid motions in the velocity field of turbulent unstratified NCBLs.

Stable stratification is known to alter the mean flow and turbulent structure significantly. Ambient stable stratification is ubiquitous in many natural and industrial flows (Fan *et al.* 2021); yet, there is little research concerning NCBLs immersed in stably stratified media. Such flows arise in serval classes of natural ventilation problems where the ambient medium is often stably stratified (Bejan 2013). For example, such boundary layer flow could be observed along the interior surfaces of heated or cooled walls in

buildings where the room is stably stratified. NCBLs immersed in stably stratified media are also often discussed in connection to differentially heated cavities (Gill 1966; Gill & Davey 1969). The differentially heated cavity and its corresponding boundary layer flow form a simplified representation of the fluid flow and heat transfer in fuel tanks, cooling of electrical equipment and solar collectors. Often such NCBLs are modelled using the one-dimensional formulation proposed by Prandtl (1952), referred to as the 'buoyancy layer' from hereon. In line with previous studies (Gill & Davey 1969; McBain, Armfield & Desrayaud 2007; Fedorovich & Shapiro 2009*b*; Maryada *et al.* 2022), the current study uses the buoyancy layer to model an NCBL immersed in a stably stratified medium.

Like unstratified NCBLs, most studies on turbulent buoyancy layers focussed on the mean flow and one-point statistics (Fedorovich & Shapiro 2009*a*,*b*; Giometto *et al.* 2017). Large-scale coherence of the streamwise velocity field was hinted by Schumann (1990). Schumann (1990) showed that large-scale coherence could exist in the outer layers of inclined and upright turbulent buoyancy layers using LES. For the vertical case, large-scale coherence of streamwise velocity was observed in the streamwise direction. For inclination angles where the heated surface was close to the horizontal, large-scale coherence was observed in the spanwise direction. However, limited conclusions can be drawn regarding the properties of LSMs resulting from such large-scale coherence due to the computational limitations of the study of Schumann (1990).

1.1. *Contributions of the present study*

It is evident from the above literature that, despite being investigated for the better part of the last century, there is still no clear consensus on whether the LSMs are always present in NCBLs (both with and without stably stratified ambient media) and, if present, how they compare with LSMs in canonical wall-bounded turbulence. In an effort to clarify this long-standing issue, the existence of LSMs in a turbulent buoyancy layer is examined using DNS. An illustration of the problem at hand with the key findings is shown in figure 1.

The buoyancy layer is defined in § 2 along with the computational details of the DNS.

The coherence, using two-point correlations, is investigated in § 3.2 where it is shown that the LSMs of streamwise velocity fluctuations are dominant in the outer layer of the buoyancy layer.

Unlike what is observed in unstratified NCBLs (Hattori *et al.* 2006), the two-point correlations of streamwise velocity fluctuations exhibit signs of meandering, and this is examined in § 3.2.2. Here, it is demonstrated that the meandering is correlated with the sign of the spanwise velocity fluctuations.

The wall-normal coherence of LSMs is investigated in § 3.2.3. It is shown that the streamwise velocity fluctuations are coherent across significant wall-normal distances in the buoyancy layer, implying that large-scale eddies are dominant in vertical buoyancy layers.

The role of LSMs in TKE production is discussed in § 3.2.4. It is demonstrated that the LSMs, especially in the outer layer, are dynamically relevant and make considerable contributions towards the production of TKE.

Section 3.3 discusses the one-dimensional energy spectra of streamwise velocity fluctuations, where it is revealed that LSMs are the dominant energy-containing motions in the turbulent buoyancy layer.

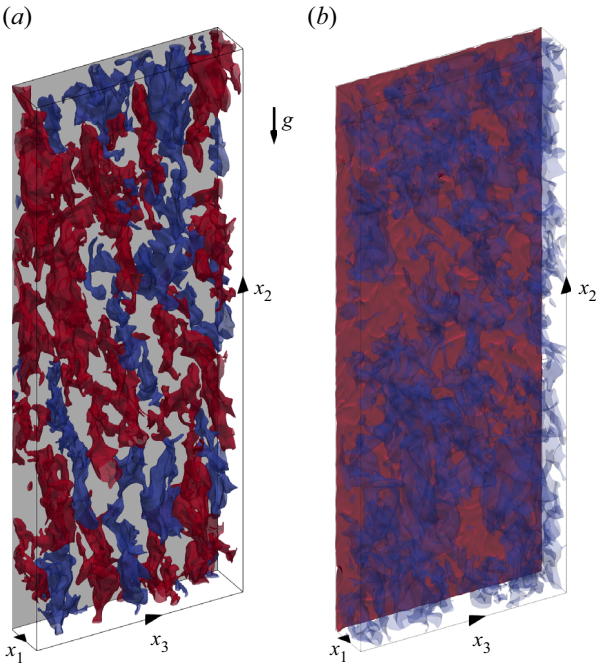

Figure 1. An illustration of the problem at hand. (*a*) The high-speed (red contours represent the streamwise velocity perturbations $u_2 = 2u_\tau$, with u_τ being the friction velocity as defined in § 2) and low-speed (blue contours represent the streamwise velocity perturbations $u_2 = -2u_\tau$) LSMs in a turbulent buoyancy layer. The grey surface represents the heated wall with $\tilde{\vartheta} = 1$. (*b*) The non-dimensional temperature $\tilde{\vartheta}$ contours at $\tilde{\vartheta} = 0.7$ (red) and $\tilde{\vartheta} = -0.05$ (blue). Here, x_1, x_2 and x_3 are the wall-normal, streamwise and spanwise directions, respectively. The flow flows along the positive x_2 axis while the acceleration due to gravity $\boldsymbol{g}$ acts along the negative x_2 axis.

2. Computational details

Let us consider a linearly heated vertical wall immersed in a stably stratified environment (positive vertical temperature gradient) such that the temperature difference (ΔT) between the heated wall (having temperature T_w) and the ambient medium (having temperature T_∞) is a constant value ($\Delta T = T_w - T_\infty = B$, where B is an arbitrary constant). As the ambient medium has a positive vertical temperature gradient, the wall temperature must also increase similarly in the vertical direction to ensure $\Delta T = B$. This implies that T_w and T_∞ are functions of the vertical coordinate x_2. Here, following (Janssen & Armfield 1996; McBain *et al.* 2007; Zhao *et al.* 2016, 2017; Maryada *et al.* 2022), we define x_1, x_2 and x_3 as the wall-normal, streamwise and spanwise directions, respectively. If $\Delta T = B$, an equilibrium NCBL with a constant boundary layer thickness develops on the heated surface, termed the buoyancy layer (Prandtl 1952). The current study uses this to model an NCBL immersed in a stably stratified medium.

The flow is non-dimensionalised with the following velocity ($U_{\Delta T}$) and length (δ_l) scales (Gill & Davey 1969):

$$U_{\Delta T} = \Delta T \left(\frac{\boldsymbol{g}\beta\kappa}{\nu\gamma_s} \right)^{1/2}, \tag{2.1a}$$

$$\delta_l = \left(\frac{4\nu\kappa}{\boldsymbol{g}\beta\gamma_s} \right)^{1/4}, \tag{2.1b}$$

where the thickness of the boundary layer is of the order of δ_l. Here, $\nu, \kappa, \boldsymbol{g}, \beta, \gamma_s$ are the kinematic viscosity, thermal diffusivity, acceleration due to gravity, coefficient of thermal expansion and the positive vertical temperature gradient, respectively. The magnitude of γ_s defines the level/strength of stable stratification in the flow. As the ambient is stably stratified due to a positive vertical temperature gradient, let us assume $T_\infty = \gamma_s x_2$ and $T_w = B + \gamma_s x_2$ such that $\Delta T = B$ (Gill 1966). Also, let us define $\tilde{\vartheta} = (T - T_\infty)/\Delta T$, which is the temperature excess over the positive vertical temperature gradient scaled with ΔT (Gill & Davey 1969; McBain *et al.* 2007). The buoyancy frequency N is $\sqrt{g\beta\gamma_s}$. Based on this non-dimensionalisation, the Reynolds number is defined as $Re = U_{\Delta T}\delta_l/\nu = (g\beta\Delta T\delta_l^3)/2\nu^2$. It should be noted that the Reynolds number is half the Grashof number ($Gr = 2Re = g\beta\Delta T\delta_l^3/\nu^2$) in the current non-dimensionalisation (Gill & Davey 1969).

With the above non-dimensionalisation, the following non-dimensional Navier–Stokes equation with the Oberbeck–Boussinesq approximation for buoyancy and the scalar transport equation are used to solve for the buoyancy layer (Gill & Davey 1969; McBain *et al.* 2007; Maryada *et al.* 2022)

$$\frac{\partial \tilde{u}_i}{\partial x_i} = 0, \tag{2.2a}$$

$$\frac{\partial \tilde{u}_i}{\partial t} + \tilde{u}_j \frac{\partial \tilde{u}_i}{\partial x_j} = -\frac{\partial \tilde{p}}{\partial x_i} + \frac{1}{Re}\frac{\partial^2 \tilde{u}_i}{\partial x_j^2} + \frac{2}{Re}\tilde{\vartheta}\,\delta_{i2}, \tag{2.2b}$$

$$\frac{\partial \tilde{\vartheta}}{\partial t} + \tilde{u}_j \frac{\partial \tilde{\vartheta}}{\partial x_j} = \frac{1}{Re\,Pr}\frac{\partial^2 \tilde{\vartheta}}{\partial x_j^2} - \frac{2}{Re\,Pr}\tilde{u}_2, \tag{2.2c}$$

where $\tilde{\vartheta}$ is the instantaneous non-dimensional temperature, also called the buoyancy field (as defined in the previous paragraph), $\tilde{u}_i$ is the instantaneous non-dimensional velocity field, $\tilde{p}$ is the instantaneous pressure field, and $Pr = \nu/\kappa$ is the Prandtl number of the fluid. For the current non-dimensionalisation, the buoyancy time period ($T_{SB} = \pi Re\sqrt{Pr}$) (Gill & Davey 1969; McBain *et al.* 2007) is 2117.22.

Figure 2 shows the coordinate system and a schematic of the NCBL in the relevant non-dimensional variables. It is evident from the figure that the stably stratified ambient medium causes the boundary layer to develop regions of flow reversal and $\tilde{\vartheta}$ deficit, which are notably absent in unstratified NCBLs. The wall-normal distance between the linearly heated wall ($\tilde{\vartheta} = 1$) and the location where the mean streamwise velocity changes sign for the first time (represented using a dashed vertical line in figure 2) is termed the boundary layer thickness δ_{bl}. This definition is chosen as the mean flow does not asymptotically reach zero in the current flow, like unstratified NCBLs. Instead, due to the presence of a flow reversal, there is a well-defined location where the mean flow becomes zero and changes sign, allowing for a precise calculation of δ_{bl} based on the mean flow (this is also discussed in § 3.1).

Throughout this paper, the instantaneous velocity and buoyancy fields are represented using $\tilde{u}_i$ and $\tilde{\vartheta}$, respectively. Using Reynolds decomposition, the instantaneous fields are decomposed into the mean flow and fluctuating fields/perturbations. The mean flow fields are represented using $\bar{\cdot}$ and consequently, the mean streamwise velocity and buoyancy fields are indicated using $\overline{u_2}$ and $\bar{\vartheta}$, respectively. The fluctuating velocity and temperature fields are represented using u_i and ϑ (such that $\tilde{u}_i = \overline{u_i} + u_i$ and $\tilde{\vartheta} = \bar{\vartheta} + \vartheta$). Averaged quantities of one-point turbulence statistics and correlations are represented using $\langle\cdot\rangle$. For the mean flow profiles and one-point turbulence statistics, the flow is averaged in time and

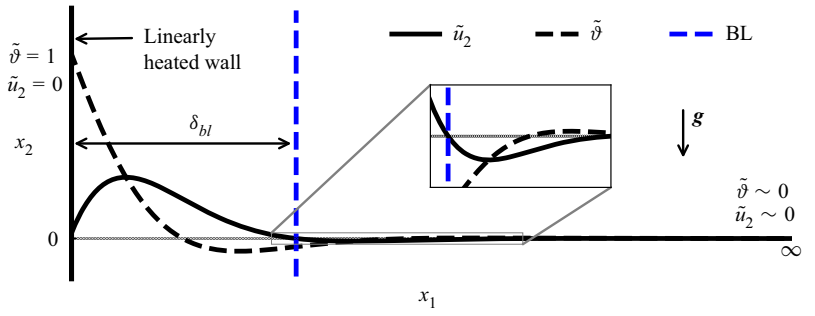

Figure 2. The schematic representation of the vertical buoyancy layer showing the coordinate system and boundary conditions. Here, $\tilde{u}_2$ is the streamwise velocity, and $\tilde{\vartheta}$ is the buoyancy field, the non-dimensional temperature field. The boundary layer thickness δ_{bl} is the wall-normal distance between the linearly heated wall and the blue dashed vertical line marked as BL. The inset shows the zoomed view of the flow reversal where $\tilde{u}_2$ is negative.

the homogeneous streamwise (x_2) and spanwise (x_3) directions. The required quantities are averaged in time and the corresponding directions for the correlations.

A turbulent vertical buoyancy layer having a Prandtl number of 0.71 and a Reynolds number of 800 is investigated using DNS. It corresponds to a friction Reynolds number $Re_\tau = u_\tau \delta_{bl}/\nu = 279.3$, where the boundary layer thickness is represented by δ_{bl}, determined as the location where the mean streamwise velocity ($\overline{u_2}$) changes sign for the first time (shown in figure 2). The friction velocity is represented using $u_\tau = \sqrt{\nu \partial \overline{u_2}/\partial x_1|_w}$ (Ke *et al.* 2020). Here, the subscript w indicates that the derivative is calculated at the wall.

Along with Re_τ, let us define $\delta^{L_m} = \delta_{bl}/L_m$, which represents the ratio of the boundary layer thickness to $L_m = \nu^{3/4} F_s^{-1/4}$. The buoyancy flux at the heated wall is represented using $F_s = -\alpha \partial \bar{\vartheta}/\partial x_1|_w$ and L_m is analogous to the Kolmogorov length scale (Fedorovich & Shapiro 2009*a*,*b*; Giometto *et al.* 2017). This can be considered as the ratio of the length scale of the eddies that scale with δ_{bl} to the length scale of the eddies that scale with L_m, and provides an estimate on the range of scales present in the flow. In terms of δ^{L_m} ($\delta^{L_m} \approx 400$ in the present case), the Reynolds number of 800 investigated in the current study is comparable to the range of parameters investigated in (Fedorovich & Shapiro 2009*b*; Giometto *et al.* 2017). Developed turbulence was observed at these values of δ^{L_m} (Fedorovich & Shapiro 2009*b*).

In the context of zero pressure gradient turbulent boundary layers, this Re_τ can be considered low to moderate, and LSMs are seldom observed at such values of Re_τ (Hutchins & Marusic 2007; Smits *et al.* 2011; Marusic & Adrian 2012). However, that is not the case for the turbulent buoyancy layer. It is demonstrated in § 3 that this friction Reynolds number is sufficient to observe LSMs in the turbulent buoyancy layer. It should be noted that the LSMs are defined as motions whose streamwise length scales exceed the boundary layer thickness, in line with canonical wall-bounded turbulence literature (Lee *et al.* 2014, 2015; Hwang *et al.* 2016).

DNS was performed using an in-house non-staggered finite volume code (Norris 2000; Armfield *et al.* 2003). The code has been used extensively to investigate natural convection flows, and its verification and validation are well documented (Armfield *et al.* 2003; Maryada *et al.* 2022). The spatial terms were discretised using a second-order central difference scheme. Temporally, the advection and the diffusion terms were discretised using a second-order Adams–Bashforth scheme (Lilly 1965) and a second-order Crank–Nicolson scheme, respectively. A non-iterative fractional step method

was used to solve for continuity (Armfield & Street 2002). Collocated meshes are known to be susceptible to spurious oscillations in the pressure field, and Rhie–Chow interpolation (Rhie & Chow 1983) was used to avoid them. Rhie–Chow interpolation or related schemes retain the grid-scale ellipticity (Armfield 1994; Armfield *et al.* 2003), thereby avoiding the grid-scale oscillations in the pressure field. The velocity and scalar equations were solved using a generalised minimal residual (Saad & Schultz 1986) algorithm with a Jacobi preconditioner. The pressure Poisson equation was solved using the bi-conjugate gradient stabilised algorithm (van der Vorst 1992) with the strongly implicit procedure of Stone (1968) as a preconditioner. An appropriate time step was chosen such that the Courant number was always less than 0.2. Also, the divergence of the velocity field was checked after every time step and was always below 5×10^{-10}.

As the turbulent buoyancy layer is spatially homogeneous in the streamwise and spanwise directions, periodic boundary conditions were imposed in the streamwise and spanwise directions, in line with previous studies (Fedorovich & Shapiro 2009*b*; Giometto *et al.* 2017; Maryada *et al.* 2022). A no-slip boundary condition for velocity ($\tilde{u}_i = 0$) and a constant buoyancy ($\tilde{\vartheta} = 1$) boundary condition were used at the heated wall. An open-type boundary condition where the flow can enter and exit the domain was used as the far-field boundary condition. At the open-type boundary, a zero gradient boundary condition normal to the boundary was applied for all the variables. In cases when flow enters the domain, it was set to have a constant temperature of $\tilde{\vartheta} = 0$, which corresponds to the flow as $x_1 \to \infty$ (see figure 2). This boundary condition was also used while investigating transitional buoyancy layers (Maryada *et al.* 2022).

The computational domain is $2.18\pi\delta_{bl} \times 8\pi\delta_{bl} \times 3\pi\delta_{bl}$ in the wall-normal (x_1), streamwise (x_2) and spanwise directions (x_3), respectively. In the wall-normal direction, the domain is bigger than the recommended wall-normal domain size of $3\delta_{bl}$ often employed in DNS of boundary layer flows (Schlatter & Örlü 2010; Kozul, Chung & Monty 2016; Ke *et al.* 2021). Due to the large domain size, the boundary conditions at the far-field wall-normal domain boundary are not expected to affect the boundary layer flow. The domain size is similar to the domain size of Bae & Lee (2021) in the streamwise and spanwise directions and bigger than the domains previously used to investigate turbulent buoyancy layers (Schumann 1990; Giometto *et al.* 2017). It should be noted that the domain size in the streamwise and spanwise directions is sufficient for the computed two-point correlations to decay to zero (evident from the results presented in § 3). This ensures that the numerical simulation results are not influenced by the periodic boundary conditions (Moin & Kim 1982).

The domain has $350 \times 1400 \times 550$ cells along the wall-normal (x_1), streamwise (x_2) and spanwise (x_3) directions, respectively. Uniform grids were used in the streamwise and spanwise directions with $\Delta x_2^+ = \Delta x_3^+ = 4.95$, where Δ is the thickness of the cell. A semi-logarithmic mesh with a stretching factor of 1.01 was used in the wall-normal direction with $\Delta x_1^+ = 0.42$ at the wall and $\Delta x_1^+ = 3.25$ at $x_1 = \delta_{bl}$. The distances represented with $^+$ are normalised by the viscous length scale ($\delta_\nu = \nu/u_\tau = 0.042$). The mesh spacing employed is similar to the spacing commonly used in DNS of canonical wall-bounded turbulence and NCBLs (Hwang *et al.* 2016; Ke *et al.* 2020; Bae & Lee 2021; Ke *et al.* 2021). The Kolmogorov length scale $\eta = (\nu^3/\epsilon)^{1/4}$ was calculated *a posteriori* and it was found that $\Delta x_1 < \eta$, $\Delta x_2 < 3\eta$ and $\Delta x_3 < 3\eta$ everywhere inside the boundary layer. Here, $\epsilon = \nu\langle(\partial u_i/\partial x_j)(\partial u_i/\partial x_j)\rangle$ is the dissipation (Giometto *et al.* 2017). It should be noted that η is a function of the wall-normal distance (as ϵ is a function of the wall-normal distance), and the values of $\Delta x_i/\eta$ reported earlier represent the 'worst case'

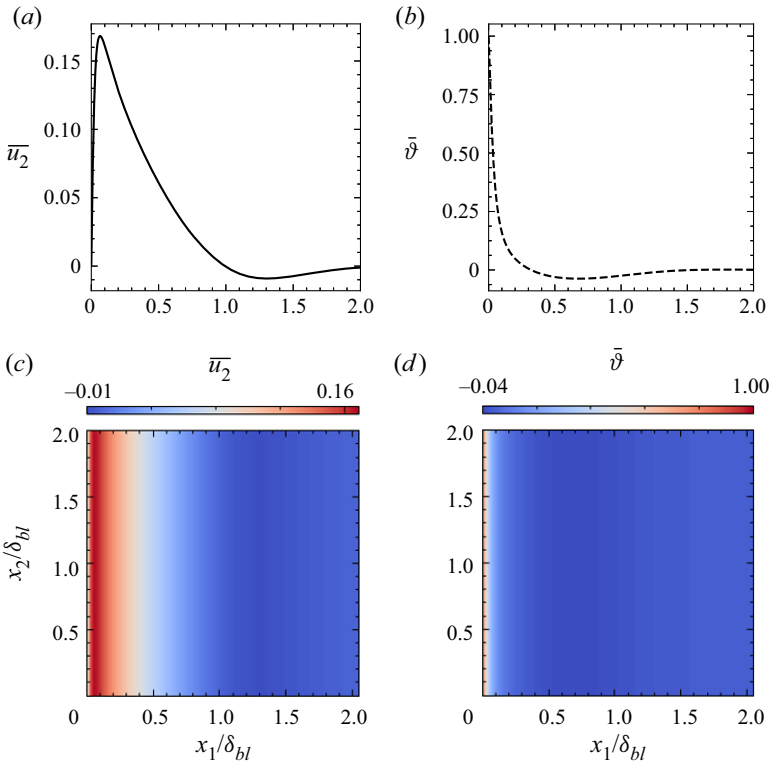

Figure 3. Profiles of (*a*) mean streamwise velocity $\overline{u_2}$ and (*b*) mean buoyancy $\bar{\vartheta}$ fields of the vertical buoyancy layer at $Re = 800$. The contours of $\overline{u_2}$ and $\bar{\vartheta}$ are shown in (*c*) and (*d*), respectively.

grid sizes. At the heated wall, $\eta = 0.074$ ($\eta/L_m \approx 2.5$), and $\Delta x_1 < 0.25\eta$, $\Delta x_2 < 3\eta$ and $\Delta x_3 < 3\eta$.

The DNS was run for nine buoyancy periods, and the statistics were calculated for the last four buoyancy periods. No significant differences were observed in the mean flow and turbulence statistics between the flow averaged for three and four buoyancy periods, indicating statistical convergence. It should be noted that the time period used to calculate statistics is in the range of values used by Giometto *et al.* (2017) for the turbulent buoyancy layer.

3. Results and discussion

3.1. *Mean flow and turbulence statistics*

Visualising the averaged mean flow and one-point statistics is worthwhile before investigating LSMs. The one-dimensional mean streamwise velocity and temperature profiles and their respective contour plots are shown in figure 3. In the figure, the boundary layer thickness, δ_{bl}, is defined as the wall-normal distance from the heated wall until the location where the mean streamwise velocity changes sign for the first time. It is clear from the figure that the mean streamwise velocity and buoyancy fields are qualitatively similar to the schematic shown in figure 2. The mean buoyancy field exhibits a region of temperature deficit while there is a distinct region of flow reversal in the mean streamwise velocity field (Schumann 1990; Fedorovich & Shapiro 2009*a*,*b*; Giometto *et al.* 2017). The region of flow reversal extends in the range $1.0 \leq x_1/\delta_{bl} \leq 2.0$ in figure 3(*a*,*c*). The region of temperature

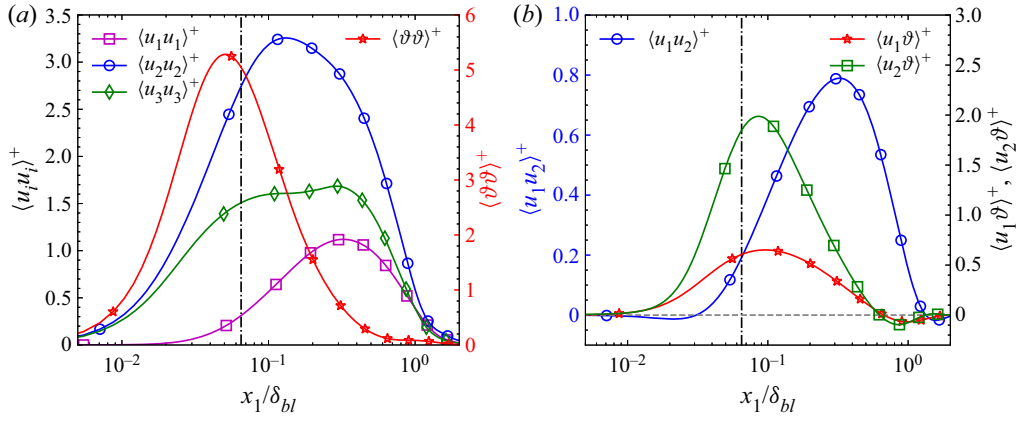

Figure 4. One-point statistics of the turbulent vertical buoyancy layer at $Re = 800$. (*a*) Mean velocity and buoyancy variances, and (*b*) mean Reynolds shear stress and wall-normal and streamwise turbulent heat fluxes. The dot-dashed black vertical line in both figures refers to the location of the velocity maximum, demarcating the inner layer from the outer layer. In (*a*), the vertical axis on the left corresponds to velocity variances, while the axis on the right corresponds to buoyancy variance. In (*b*), the vertical axis on the left corresponds to Reynolds shear stress, while the axis on the right corresponds to wall-normal and streamwise turbulent heat flux.

deficit is observed in the range $0.3 < x_1/\delta_{bl} < 1.5$ in figure 3(*b*,*d*). The inner layer is classified as the wall-normal region between the heated wall and the wall-normal location where the mean streamwise velocity is maximum ($0 < x_1/\delta_{bl} \leq 0.065$). The outer layer is defined as the wall-normal region between the wall-normal location where the mean streamwise velocity is maximum and the flow reversal ($0.065 < x_1/\delta_{bl} \leq 1.0$). These plots demonstrate that the buoyancy layer is distinctly different from unstratified NCBLs where flow reversal and temperature deficit regions are not observed (Tsuji & Nagano 1988*a*; Abedin, Tsuji & Hattori 2009; Ke *et al.* 2020, 2021).

The variances of wall-normal, streamwise and spanwise velocity and buoyancy fluctuations are shown in figure 4(*a*). In the figure, the velocity variances are normalised using the square of the friction velocity (u_τ^2) and the buoyancy variance is normalised using the square of the friction temperature (θ_τ^2). The definitions of u_τ and θ_τ are consistent with Ke *et al.* (2020, 2021). The mean streamwise velocity variance is greater than the wall-normal and spanwise velocity variance, suggesting that the streamwise velocity variance is the dominant contributor of TKE, as expected in turbulent boundary layer flows. Flow anisotropy is also evident from figure 4(*a*), hinting at the multiscale nature of the flow. The variance of all the velocity fluctuations exhibits a maximum in the outer layer at the Reynolds number investigated, implying that most of the turbulence associated with momentum transfer is present in the outer layer of the buoyancy layer. The peak in the streamwise velocity variance in the outer layer corresponds to a peak in the energy spectra of streamwise velocity fluctuations, which is discussed in § 3.3. In the inner layer, the variance of wall-normal velocity fluctuations decays faster than the variance of streamwise and spanwise velocity fluctuations and buoyancy fluctuations due to the presence of a wall.

In contrast, the peak of the buoyancy variance is located in the inner layer close to the velocity maximum. This is the case as strong buoyancy gradients occur in this region (Fedorovich & Shapiro 2009*b*; Giometto *et al.* 2017). In the wall-normal direction, the buoyancy variance decays faster than the velocity variances, implying that most buoyancy fluctuations are restricted to regions close to the heated wall, consistent with

the observations of Giometto *et al.* (2017). This behaviour of velocity and buoyancy variances also agrees with what is observed in transitional buoyancy layers (Maryada *et al.* 2022). Also, it is qualitatively similar to what is observed in turbulent differentially heated channels and unstratified NCBLs, where a peak in the streamwise velocity variance is observed in the outer layer (Tsuji & Nagano 1988*b*; Abedin *et al.* 2009; Ng *et al.* 2017). These plots highlight the stark differences between the present flow configuration and canonical wall-bounded turbulence. At comparable values of Re_τ, in canonical wall-bounded turbulence, there is a distinct peak in velocity variances close to the wall due to the inner wall cycle. An inner peak is absent in the present case, and turbulence is present mainly in the outer layer.

The wall-normal variation of Reynolds shear stress and the wall-normal and streamwise turbulent heat fluxes are shown in figure 4(*b*). Here, the Reynolds shear stress is normalised using u_τ^2, and the turbulent heat fluxes are normalised using $\theta_\tau u_\tau$. The Reynolds shear stress is negative close to the wall in the inner layer and becomes positive with increasing wall-normal distance, in agreement with the observations of Fedorovich & Shapiro (2009*b*) and Giometto *et al.* (2017). Similar behaviour is observed in unstratified NCBLs and turbulent differentially heated channels (Ke *et al.* 2020; Kim *et al.* 2021). A region of approximately constant Reynolds shear stress, commonly observed in turbulent boundary layers, is absent. On the other hand, the streamwise and wall-normal turbulent heat fluxes are always positive in the inner layer. These are also positive in the outer layer until $x_1 \approx 0.6\delta_{bl}$. Both the wall-normal and streamwise turbulent heat fluxes are negative from approximately this wall-normal location and beyond, which agrees with the observations of Giometto *et al.* (2017). Also, the Reynolds shear stress peaks in the outer layer at $x_1 \approx 0.3\delta_{bl}$ while the turbulent heat fluxes peak at locations much closer to the maximum velocity (still in the outer layer). The Reynolds shear stress and streamwise turbulent heat flux feature in the production of TKE. The production of TKE in relation to LSMs is discussed in § 3.2.4.

3.2. *Two-point correlations*

The existence of LSMs is investigated using two-point correlations (Ganapathisubramani *et al.* 2005; Hutchins & Marusic 2007; Baltzer *et al.* 2013; Sillero, Jiménez & Moser 2014; Hwang *et al.* 2016). The two-point correlation coefficient at a wall-normal plane of a fluctuating field ϕ, $R^T_{\phi\phi}$, is calculated using

$$R^T_{\phi\phi} = \frac{\langle \phi(x_2, x_3)\phi(x_2 + \Delta x_2, x_3 + \Delta x_3)\rangle}{\sigma_\phi^2}, \tag{3.1}$$

where σ_ϕ is $\sqrt{\langle \phi^2 \rangle}$. Throughout this paper, $\Delta x_2 > 0$ corresponds to the correlation downstream of the location of interest, and the correlation upstream of the location of interest corresponds to $\Delta x_2 < 0$.

The two-point correlation coefficients of ϑ, u_1, u_2 and u_3 in the streamwise direction at four different wall-normal locations are shown in figure 5. In the figure, the two-point correlation coefficient at $x_1 = 0.04\delta_{bl}$ corresponds to a wall-normal location in the inner layer. The two-point correlations at the remaining wall-normal locations correspond to the outer layer. In the inner layer, the u_1, u_3 and ϑ fluctuations are positively correlated for $|\Delta x_2| < 1$. The u_2 fluctuations, on the other hand, exhibit a positive correlation coefficient for $|\Delta x_2| > 1$, hinting at the presence of LSMs. Qualitatively, the same conclusions also hold in the outer layer, with the width of the positive two-point correlation coefficient of u_2 being greater than the width of the positive two-point correlation coefficient of u_1, u_3

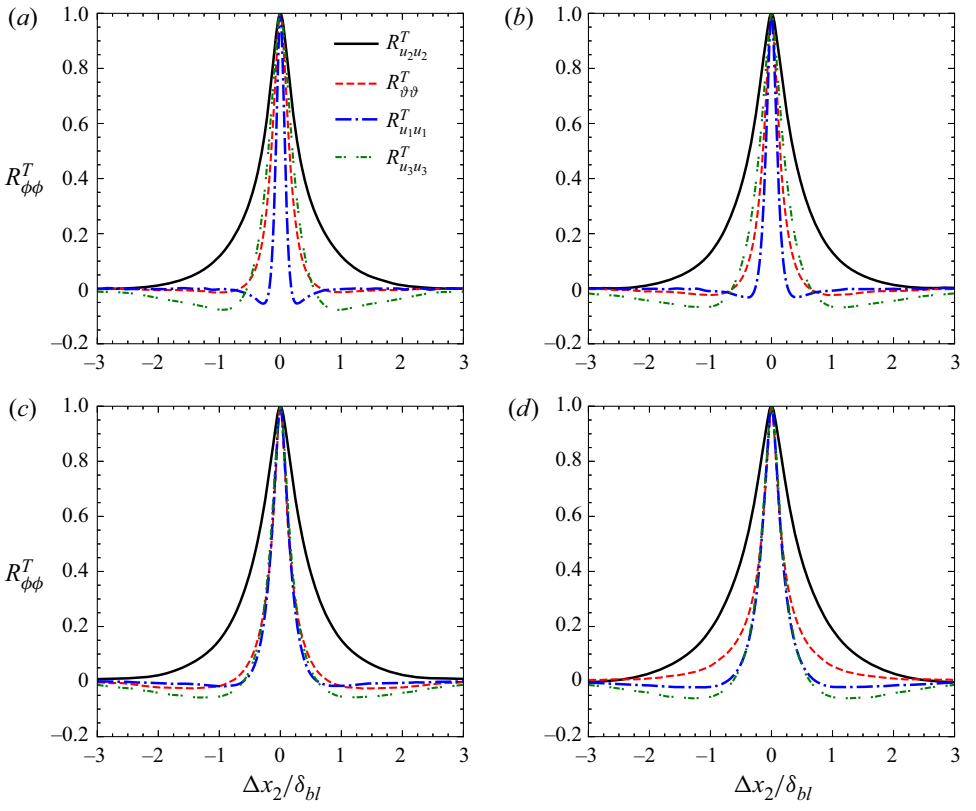

Figure 5. The $R^T_{u_2u_2}$, $R^T_{\vartheta\vartheta}$, $R^T_{u_1u_1}$, $R^T_{u_3u_3}$ correlations in the streamwise direction at (*a*) $x_1/\delta_{bl} = 0.04$, (*b*) $x_1/\delta_{bl} = 0.1$, (*c*) $x_1/\delta_{bl} = 0.3$ and (*d*) $x_1/\delta_{bl} = 0.6$. The thick solid black curve represents $R^T_{u_2u_2}$, thin red dashed curve represents $R^T_{\vartheta\vartheta}$, thick blue densely dash-dotted curve represents $R^T_{u_1u_1}$ and thin green loosely dash-dotted curve represents $R^T_{u_3u_3}$.

and ϑ. The widths of the correlation of u_1 and u_3 become comparable with increasing wall-normal distance. The buoyancy fluctuations become increasingly correlated in the streamwise direction as one moves away from the wall. Figure 5 also strongly indicates that u_1, u_2, u_3 and ϑ fluctuations exhibit different length scales. As the widths of the two-point correlations of u_1, u_3, and ϑ are not comparable to the width of $R^T_{u_2u_2}$, it can be presumed that the largest streamwise coherence is present for u_2. The width of u_2 fluctuations increases with increasing wall-normal distance, and these length scales of the u_2 fluctuations are discussed later using two-point streamwise–spanwise correlations.

The two-point correlation coefficients of ϑ, u_1, u_2 and u_3 in the spanwise direction at four different wall-normal locations are shown in figure 6. In figure 6(*a*), close to the heated wall in the inner layer, the width of positive $R^T_{u_2u_2}$ is greater than the width of positive $R^T_{\vartheta\vartheta}$, $R^T_{u_1u_1}$ and $R^T_{u_3u_3}$. However, the width of $R^T_{\vartheta\vartheta}$ becomes larger with increasing wall-normal distance, indicating that the spanwise coherence of buoyancy fluctuations becomes greater than the spanwise coherence of streamwise, wall-normal and spanwise velocity fluctuations. In the outer layer, the width of the positive correlation coefficient of u_3 and ϑ in the spanwise direction (figure 6) is comparable to the width of the positive correlation coefficient in the streamwise direction (figure 5), qualitatively similar to what is observed in unstratified NCBLs (Tsuji *et al.* 1992; Hattori *et al.* 2006).

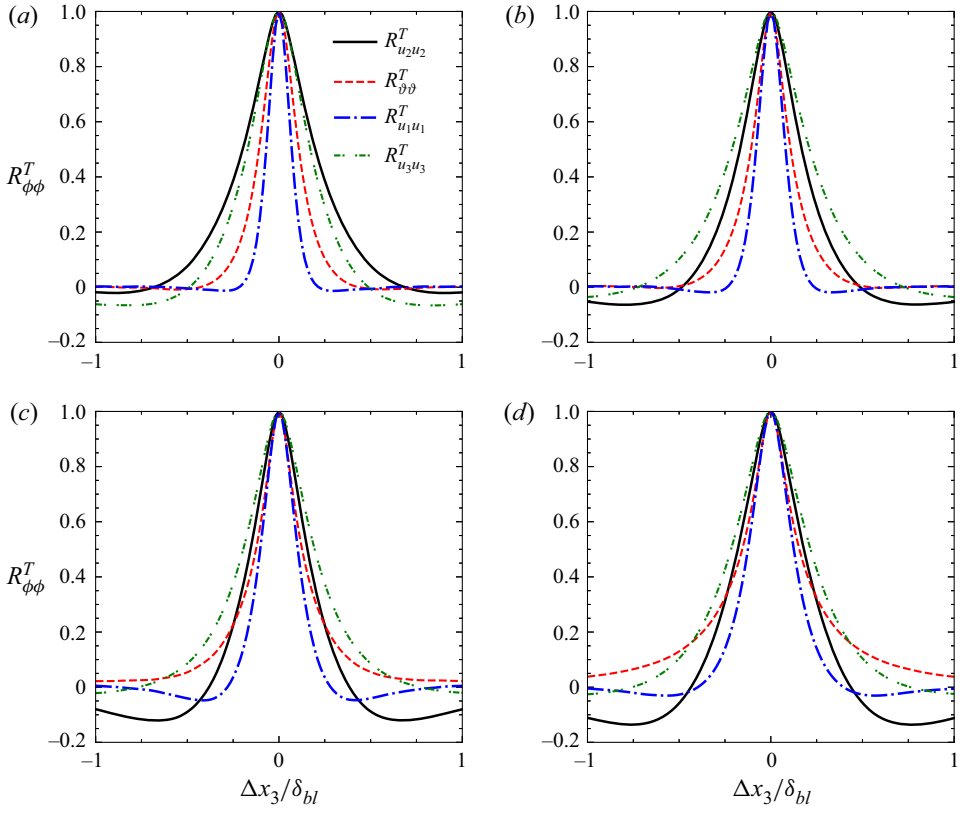

Figure 6. The $R^T_{u_2u_2}, R^T_{\vartheta\vartheta}, R^T_{u_1u_1}, R^T_{u_3u_3}$ correlations in the spanwise direction at (*a*) $x_1/\delta_{bl} = 0.04$, (*b*) $x_1/\delta_{bl} = 0.1$, (*c*) $x_1/\delta_{bl} = 0.3$ and (*d*) $x_1/\delta_{bl} = 0.6$. The thick solid black curve represents $R^T_{u_2u_2}$, thin red dashed curve represents $R^T_{\vartheta\vartheta}$, thick blue densely dash-dotted curve represents $R^T_{u_1u_1}$ and thin green loosely dash-dotted curve represents $R^T_{u_3u_3}$. Note that the horizontal scale differs from figure 5.

Despite the spanwise coherence of ϑ and u_3 extending to greater distances than the spanwise coherence of u_2, it is still smaller than the streamwise coherence of u_2. This suggests that the u_2 fluctuations statistically exhibit the most prominent coherence. Therefore, the rest of the paper investigates the large-scale coherence of the streamwise velocity fluctuations, u_2.

It should be noted that the two-point correlations of u_2 in figure 6 become negative at $|\Delta x_2| \gtrsim 0.5\delta_{bl}$, which is absent in the two-point correlations of u_2 in the streamwise direction (see figure 5). Negative values of two-point correlations of u_2 in figure 6 suggest that alternating fast-moving and slow-moving structures are present in the flow. This is investigated in detail later in this section using streamwise–spanwise two-point correlations.

It should be stressed that the profiles of the two-point correlations of buoyancy fluctuations do not match the profiles of two-point correlations of the streamwise velocity fluctuations. It implies that relying on two-point correlations of the temperature field to investigate large-scale coherent motions in turbulent buoyancy layers would provide an incomplete picture of the boundary layer structure.

The long tails of two-point correlation coefficients merely suggest the presence of large-scale coherence. However, this does not provide insight into whether the large-scale

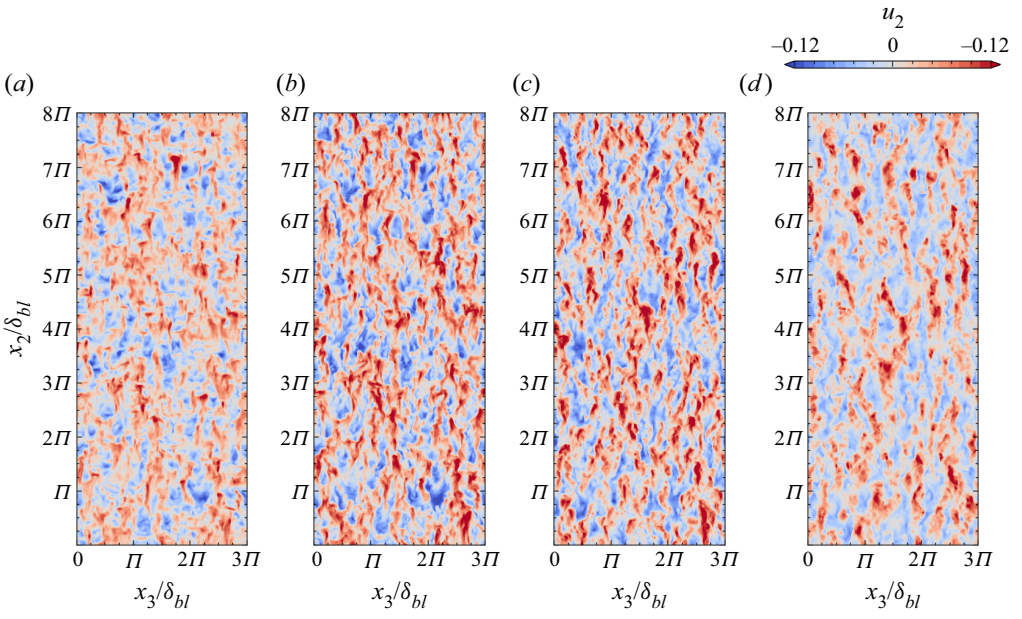

Figure 7. Instantaneous streamwise velocity fluctuations at (*a*) $x_1/\delta_{bl} = 0.04$, (*b*) $x_1/\delta_{bl} = 0.1$, (*c*) $x_1/\delta_{bl} = 0.3$ and (*d*) $x_1/\delta_{bl} = 0.6$. Gravity acts in the negative x_2 direction, and the fluid flows in the positive x_2 direction. High-speed velocity fluctuations refer to positive streamwise velocity fluctuations, and low-speed velocity fluctuations refer to negative streamwise velocity fluctuations.

coherence is due to LSMs or a chain of several small-scale structures (Sillero *et al.* 2014). Hence, examining the instantaneous flow structures helps us to understand the distribution of streamwise velocity perturbations. The instantaneous streamwise velocity perturbations at four different wall-normal locations are shown in figure 7. Streamwise-elongated streaky structures of high- and low-speed fluctuations dominate the figure. A high-speed velocity fluctuation refers to a positive streamwise velocity fluctuation, and a low-speed velocity fluctuation refers to a negative streamwise velocity fluctuation. The streamwise length of the u_2 often exceeds the boundary layer thickness, consistent with the two-point correlations. This suggests that the large-scale coherence observed earlier in figure 5 is due to LSMs.

Figure 7 also demonstrates that multiple scales of motion are present in high- and low-speed streamwise velocity fluctuations, similar to the multiple scales observed in canonical wall-bounded turbulence (Monty *et al.* 2007; Baltzer *et al.* 2013). In this context, the multiple scales of motion refer to large-scale and fine-scale streamwise velocity perturbations.

It can be visually inferred from figure 7 that the magnitude of the positive streamwise velocity fluctuations is generally greater than that of the negative streamwise velocity fluctuations with increasing wall-normal distance. This difference disappears as one moves towards the wall. At $x_1/\delta_{bl} = 0.6$, the flow field is dominated by intense positive streamwise velocity perturbations. Positive velocity perturbations are also present at $x_1/\delta_{bl} = 0.04$, $x_1/\delta_{bl} = 0.1$ and $x_1/\delta_{bl} = 0.3$, but their magnitude is similar to the magnitude of the negative velocity perturbations.

To quantify the distribution of streamwise velocity perturbations, the skewness $sk = u_2^3/\langle u_2 u_2\rangle^{3/2}$ of the streamwise velocity fluctuations is calculated, and its wall-normal variation is shown in figure 8. The skewness is a measure of asymmetry and indicates the

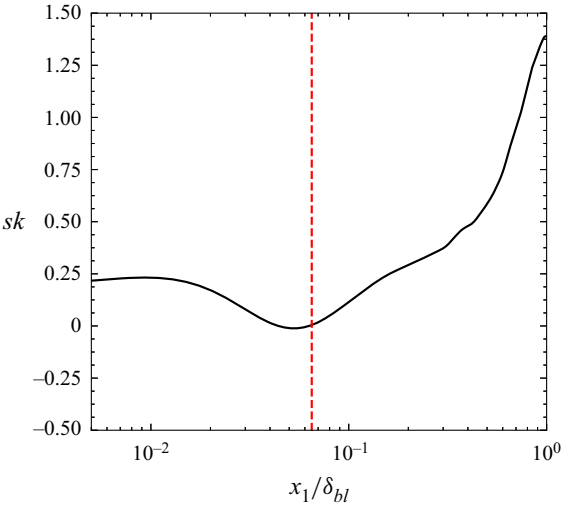

Figure 8. Wall-normal variation of the skewness (sk) of streamwise velocity fluctuations. The dashed red line represents the wall-normal location of the velocity maximum, which is used to demarcate the inner and the outer layers.

deviation of a distribution from a symmetric distribution. Positive skewness indicates that the magnitude of the intense positive fluctuations is greater than that of the intense negative ones. The opposite is true for negative values of skewness. The streamwise velocity fluctuations are positively skewed for almost the entire buoyancy layer. The skewness is positive near the wall and approaches zero at the edge of the inner layer. Here, the magnitude of the skewness is minimal, suggesting that the distribution of the streamwise velocity fluctuations is close to Gaussian, with intense positive fluctuations only being marginally more likely than intense negative fluctuations. In the outer layer, the skewness increases with increasing wall-normal distance. Until $x_1 \leq 0.5\delta_{bl}$, there is a moderate increase in the skewness value; however, at $x_1 > 0.5\delta_{bl}$, the skewness rises rapidly, reaching values greater than one at the edge of the buoyancy layer. This demonstrates that positive streamwise velocity fluctuations are more intense in magnitude than negative streamwise velocity fluctuations. As the cross-correlation between streamwise velocity fluctuations and wall-normal velocity fluctuations is the Reynolds shear stress, and the cross-correlation between streamwise velocity fluctuations and buoyancy fluctuations is the streamwise turbulent heat flux, this asymmetry would mean an asymmetric contribution to Reynolds shear stress and streamwise turbulent heat flux, which is discussed in detail in § 3.2.4.

The skewness in the outer layer is qualitatively similar to that observed near the edge of the unstratified NCBLs (Tsuji & Nagano 1988*b*; Abedin, Tsuji & Kim 2017). Comparing this plot with the wall-normal variation of skewness of streamwise velocity fluctuations in zero and adverse pressure gradient boundary layers highlights the stark differences between the turbulent buoyancy and boundary layers. In turbulent boundary layers, the skewness is negative and decreases with increasing wall-normal distance (Monty, Harun & Marusic 2011), opposite to what is observed here.

At $x_1/\delta_{bl} = 0.6$, the skewness is greater than 0.5, implying that at this wall-normal location, positive streamwise velocity fluctuations are significantly more intense than negative streamwise velocity fluctuations, confirming our interpretation of the visualisation in figure 7. This would mean that conditional sampling of the data obtained

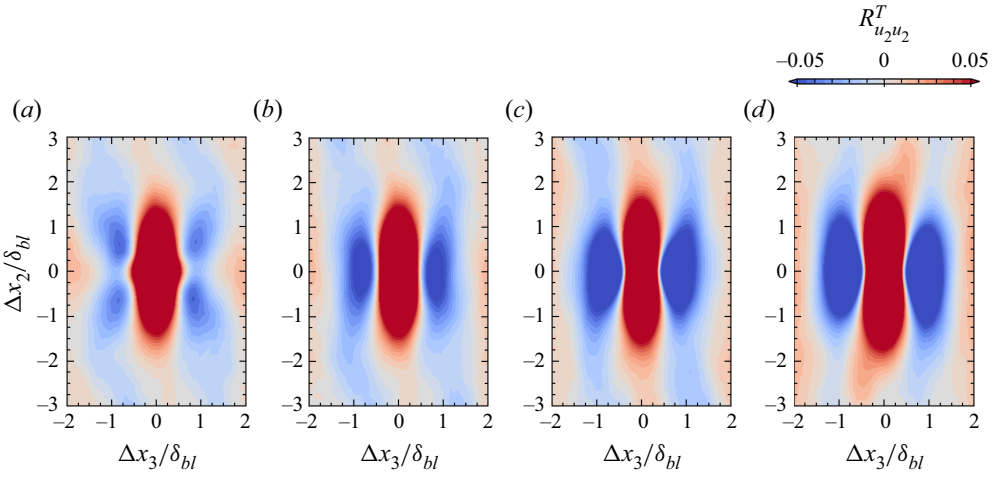

Figure 9. Streamwise–spanwise two-point correlation coefficient $R^T_{u_2u_2}$ map at (*a*) $x_1/\delta_{bl} = 0.04$ (*b*) $x_1/\delta_{bl} = 0.1$, (*c*) $x_1/\delta_{bl} = 0.3$ and (*d*) $x_1/\delta_{bl} = 0.6$.

from DNS or experiments to identify three-dimensional structures using a relatively high threshold would always bias the conditional structures to high-speed motions in the outer layer. Equivalent observations regarding conditional sampling of LSMs were made by Sillero *et al.* (2014) while investigating large-scale coherence in turbulent boundary layers and channel flows.

Figure 9 shows the streamwise–spanwise two-point correlation coefficient map of streamwise velocity perturbation of the entire turbulent flow field at $x_1 = 0.04\delta_{bl}$, $x_1 = 0.1\delta_{bl}$, $x_1 = 0.3\delta_{bl}$ and $x_1 = 0.6\delta_{bl}$. The two-dimensional representation of $R^T_{u_2u_2}$ provides richer information on the averaged structure than the one-dimensional representation shown in figures 6 and 5. As the large-scale structures are an agglomeration of multiscale motions, Baltzer *et al.* (2013) and Lee (2017) contend that even small correlation coefficient values are essential when investigating them, and hence, are shown in the figure.

At $x_1 = 0.3\delta_{bl}$ and $x_1 = 0.6\delta_{bl}$, it is apparent from figure 9 that regions of negative correlation coefficient flank a region of the streamwise-elongated positive correlation coefficient (also evident in figure 6). This indicates that fast-moving (slow-moving) perturbations surround slow-moving (fast-moving) perturbations, aiding the view that adjacent high-speed and low-speed motions extend in the streamwise direction in the vertical buoyancy layer, similar to what is observed in canonical wall-bounded turbulence (Ganapathisubramani *et al.* 2005; Hutchins & Marusic 2007; Baltzer *et al.* 2013). It should be noted that the flanking of negatively correlated regions to the positively correlated region does not imply that the motions are always symmetric. The symmetry observed in two-point correlations is an artefact of the averaging process. In reality, the LSMs are asymmetric, as evident from the instantaneous flow fields shown in figure 7. It should be noted that similar arguments were made regarding the symmetry of LSMs in turbulent boundary layers (Kevin, Monty & Hutchins 2019).

Also, at $x_1 = 0.3\delta_{bl}$ and $x_1 = 0.6\delta_{bl}$, the two-point correlations exhibit the characteristic 'X-shaped' pattern observed in canonical wall-bounded turbulence (Hutchins & Marusic 2007; Baltzer *et al.* 2013; Lee 2017). Hutchins & Marusic (2007), while investigating turbulent boundary layers, demonstrated that the meandering of the LSMs manifests itself as an 'X-shaped' in the two-point correlations. This striking observation in the present

case suggests that the LSMs in the vertical buoyancy layer also meander appreciably in the outer layer. The meandering nature of the LSMs is discussed in § 3.2.2.

At $x_1 = 0.1\delta_{bl}$, the regions of negative correlation coefficient again flank a region of streamwise-elongated positive correlation coefficient. However, the negative correlation is much weaker than at $x_1 = 0.3\delta_{bl}$ and $x_1 = 0.6\delta_{bl}$. In the inner layer, at $x_1 = 0.04\delta_{bl}$, the two-point correlation differs from what is observed in the outer layer. A streamwise-elongated rhombus replaces the streamwise-elongated 'capsule-like' shape with its major diagonal oriented in the streamwise direction. It shows a higher degree of spanwise coherence in the inner layer than in the outer layer. Also, the positive correlation is not flanked by regions of strong negative correlation, implying the lack of prominent adjacent fast-moving (slow-moving) and slow-moving (fast-moving) perturbations.

The large-scale streamwise coherence observed here also agrees with the observations of Schumann (1990) regarding the vertical buoyancy layer. However, direct quantitative comparisons cannot be made due to the computational limitations of the study of Schumann (1990). The large-scale streamwise coherence also agrees qualitatively with the large-scale streamwise coherence of turbulent unstratified NCBLs (Lochet, Lemonnier & Doan-Kim-Son 1983; Hattori *et al.* 2006). However, Hattori *et al.* (2006) noted that the regions of the negative correlations do not flank the regions of positive correlation in the streamwise direction in the case of turbulent unstratified NCBLs, which led the authors to suggest that a streaky structure, akin to the streaky structure of canonical wall-bounded turbulence, was not evident. This is not the case for the buoyancy layer, and regions of negative correlation coefficients flank a region of positive correlation coefficient in the spanwise direction. It should be noted that the LSMs discussed in the present study differ from the Λ-shaped structures observed in transitional NCBLs (Zhao *et al.* 2017, 2019).

In figure 9, the patterns at $|\Delta x_2| \gg 0$ and $|\Delta x_3| \gg 0$ depend on the dataset used due to the lack of convergence, which is due to the finite-time average of the DNS data. However, the behaviour near the centre/equilibrium region is consistent even without statistical convergence (Baltzer *et al.* 2013; Lee 2017).

3.2.1. *High-speed and low-speed large-scale streamwise motions*

The instantaneous flow fields shown in figure 7 visually demonstrate the positive skewness of the streamwise velocity fluctuations in the outer layer. The positive skewness of streamwise velocity fluctuations (figure 8) strongly suggests that high-speed and low-speed motions have different properties, especially in the outer layer.

The two-point correlations in figure 9 demonstrate large-scale coherence. However, they do not shed any light on the nature of the large-scale coherence, i.e. whether low-speed or high-speed motions are responsible for large-scale streamwise coherence. It is also unclear from the instantaneous velocities in figure 7 whether the length scales of high-speed motions are greater/less than the length scales of low-speed motions. It is investigated here by calculating the two-point conditional correlations of the streamwise velocity fluctuations. The two-point conditional correlations of the streamwise velocity fluctuations are defined as

$$R^{CP}_{u_2u_2} = \frac{\langle u_2(x_2, x_3) > 0 \,|\, u_2(x_2 + \Delta x_2, x_3 + \Delta x_3)\rangle}{\sigma_{u_2} \,|\, \sigma_{u_2} > 0}, \tag{3.2}$$

and

$$R^{CN}_{u_2u_2} = \frac{\langle u_2(x_2, x_3) < 0 \,|\, u_2(x_2 + \Delta x_2, x_3 + \Delta x_3)\rangle}{\sigma_{u_2} \,|\, \sigma_{u_2} < 0}, \tag{3.3}$$

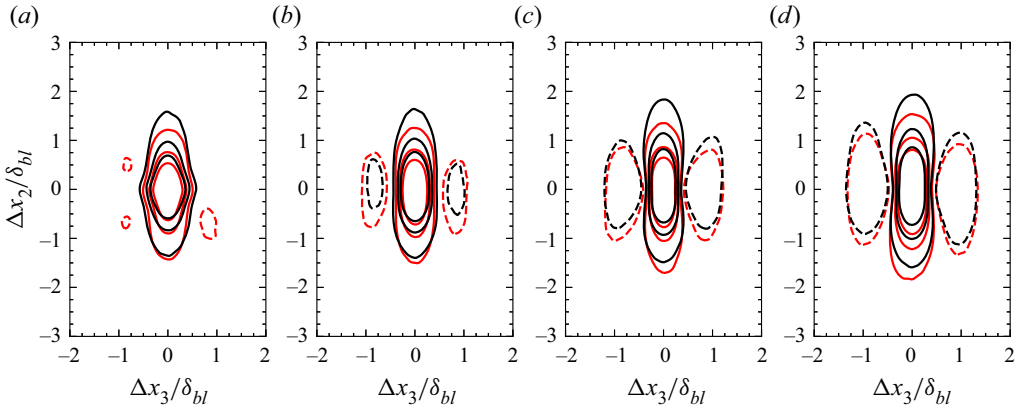

Figure 10. Streamwise–spanwise two-point conditional correlation coefficient map at (*a*) $x_1/\delta_{bl} = 0.04$ (*b*) $x_1/\delta_{bl} = 0.1$, (*c*) $x_1/\delta_{bl} = 0.3$ and (*d*) $x_1/\delta_{bl} = 0.6$. Red contours represent $R^{CP}_{u_2u_2}$ and black contours represent $R^{CN}_{u_2u_2}$. The contour lines are −0.05, 0.05, 0.15 and 0.25. Negative values are represented using dashed contours.

for positive and negative streamwise velocity fluctuations, respectively, similar to the two-point conditional correlations of Lee & Sung (2011) and Sillero *et al.* (2014).

The two-point streamwise–spanwise conditional correlation coefficients of the high-speed (positive) and low-speed (negative) streamwise velocity fluctuations at four different wall-normal locations are shown in figure 10. The two-point conditional correlation coefficients shown in the figure demonstrate that the high-speed and low-speed streamwise velocity fluctuations exhibit large-scale streamwise coherence and can form streamwise-elongated motions. The streamwise-elongated regions of positive correlations are flanked by regions of negative correlations, exhibiting similarities to the streamwise–spanwise correlation shown in figure 9. This again suggests the possibility of alternative regions of high-speed and low-speed large-scale streamwise motions, similar to the LSMs in the logarithmic layer of wall-bounded turbulence (Ganapathisubramani *et al.* 2005; Hutchins & Marusic 2007; Baltzer *et al.* 2013; Kevin *et al.* 2019). Both the conditional correlations contrast the observations of Hattori *et al.* (2006) regarding unstratified NCBLs. In that study, regions of negative two-point correlation coefficient (no conditional sampling applied) did not flank a region of positive two-point correlation coefficient (no conditional sampling applied) in the spanwise direction. The 'X-shaped' correlation pattern is also visible in the outer layer, implying the meandering nature of the LSMs. As the pattern is consistent for positive and negative streamwise velocity fluctuations, it can be inferred that both the positive and negative LSMs meander appreciably (see § 3.2.2 on the meandering of LSMs).

The two-point correlations of the positive streamwise fluctuations are biased towards the upstream direction. In contrast, the two-point correlations of the negative streamwise fluctuations are biased towards the downstream direction. This could be due to the asymmetric presence of different quadrant events in the outer layer of the buoyancy layer, similar to the asymmetry observed in turbulent boundary layers (Lee & Sung 2011). It should be noted that the positive streamwise fluctuations are biased towards the upstream direction, and the negative streamwise fluctuations are biased towards the downstream direction in turbulent boundary layers, opposite to what is observed in the present case.

In figure 10, the spatial extent of the negative correlation coefficient in the outer layer is larger than the regions of the negative correlation coefficient in the inner layer.

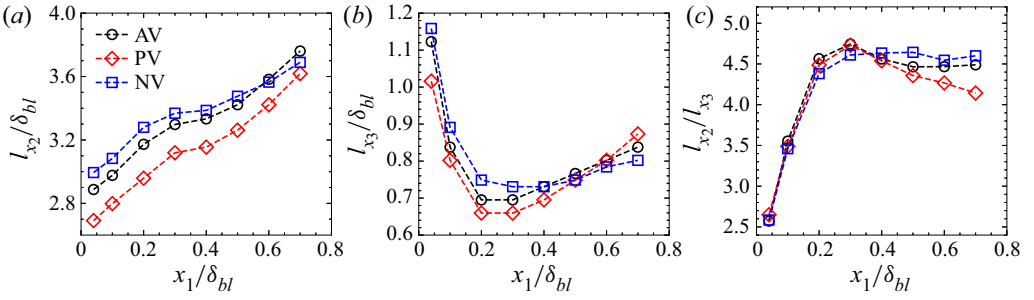

Figure 11. Wall-normal variation of the length scales of the two-point correlations. (*a*) Streamwise length scales, (*b*) spanwise length scales and (*c*) the ratio of the streamwise to the spanwise length scales; AV corresponds to the two-point correlation of the streamwise velocity fluctuations, PV corresponds to the conditional two-point correlation of positive streamwise velocity fluctuations and NV corresponds to the conditional two-point correlation of negative streamwise velocity fluctuations.

Figure 11 shows the positive two-point conditional correlations' streamwise (l_{x_2}) and spanwise length scales (l_{x_3}). The length scales are identified as regions where the two-point correlation coefficients are greater than 0.05, which aligns with the definition used in (Hutchins, Hambleton & Marusic 2005; Monty *et al.* 2007; Lee & Sung 2011, 2013; Lee 2017). The streamwise length shown in figure 11(*a*) increases with increasing wall-normal distance. This behaviour differs from what is observed in turbulent boundary layers, where the large-scale streamwise coherence, in the form of two-point correlations, peaks in the logarithmic layer and reduces in the wake region (Ganapathisubramani *et al.* 2005; Lee & Sung 2011; Sillero *et al.* 2014). It is conjectured that the interaction of the boundary layer flow with the flow reversal region generates large-scale coherence even at the edge of the boundary layer; however, it is not explored further as this interaction is outside the scope of the current study. The streamwise length of the positive streamwise velocity fluctuations is smaller than the negative streamwise velocity fluctuations, suggesting that the negative streamwise velocity fluctuations tend to form longer structures than the positive streamwise velocity structures. Despite the variation in the streamwise length scales between the positive and negative streamwise velocity fluctuations, it should be noted that the streamwise length scales at all the wall-normal distances investigated are always greater than the boundary layer thickness.

Figure 11(*b*) shows the spanwise length scales. The spanwise length of positive two-point correlations is smaller than the streamwise length of positive two-point correlations, consistent with the earlier discussion. Also, unlike the streamwise length scales, the spanwise length scale does not monotonically increase with increasing wall-normal distance.

The spanwise length is highest close to the wall, drops to a minimum at around $x_1 = 0.2\delta_{bl}$, and increases once again with increasing wall-normal distance. The spanwise length of the negative streamwise velocity fluctuations is greater than that of the positive streamwise velocity fluctuations until $x_1 < 0.5\delta_{bl}$. However, the trend reverses at $x_1 > 0.5\delta_{bl}$ with the spanwise length of the positive streamwise velocity fluctuations becoming greater than the spanwise length of the negative streamwise velocity fluctuations. It is conjectured that differences in the mean shear in the inner and the outer layers of the buoyancy layer induce changes to the spanwise scales of LSMs.

The ratio of the streamwise length to the spanwise length of the two-point correlations (l_{x_2}/l_{x_3}) is shown in figure 11(*c*). Close to the wall, l_{x_2}/l_{x_3} exhibits a minimum and increases rapidly until $x_1 \leq 0.3\delta_{bl}$. Also, close to the wall, the plot is almost identical

for positive and negative streamwise velocity fluctuations, suggesting a similarity. The ratio of the streamwise length to the spanwise length approximately attains a constant value in the outer layer for the two-point correlation of the unconditional streamwise velocity fluctuations and the two-point conditional correlation of the negative streamwise velocity perturbations. However, the ratio decreases with increasing wall-normal distance for positive streamwise velocity fluctuations, implying that the aspect ratio of the LSMs of the positive streamwise velocity fluctuations differs from the aspect ratio of the LSMs of the negative streamwise velocity fluctuations. It should be noted that the ratio is always greater than 1 for both positive and negative streamwise velocity fluctuations, signifying that the streamwise length of the two-point correlations is always greater than the spanwise length across the entire thickness of the boundary layer. This strongly implies that the LSMs are anisotropic, agreeing with the observations of Hattori *et al.* (2006) regarding unstratified vertical NCBLs.

Also, the viscous forces are not dominant in most of the outer layer at $Re = 800$ (regions where velocity variances and Reynolds shear stress are dominant – see § 3.1). This is demonstrated in Appendix A using a force balance approach, similar to the one employed in canonical wall turbulence (Fife *et al.* 2005; Wei *et al.* 2005). This suggests that the results presented regarding the LSMs in the outer layer only have marginal low-Reynolds number effects.

3.2.2. *Meandering of large-scale streamwise motions*

From the streamwise-spanwise two-point correlations shown in figures 9 and 10, especially in the outer layer, it is clear that the large-scale streamwise motions meander significantly in the spanwise direction. The streamwise velocity fluctuations shown in figure 7 also reveal that the LSMs are not perfectly aligned in the streamwise direction and are offset diagonally, exhibiting signs of meandering motion.

In this section, motivated by the analysis of Sillero *et al.* (2014) and de Silva *et al.* (2018), the meandering of LSMs is investigated in relation to the fluctuating spanwise velocity. To this end, the two-point correlation coefficients of the streamwise velocity fluctuations conditioned on the signs of streamwise and spanwise velocity fluctuations are calculated. The two-point conditional correlations of high-speed and low-speed motions of the streamwise velocity fluctuations are analogous to the two-point conditional correlations shown in (3.2) and (3.3), except that they are also conditioned based on the sign of spanwise velocity fluctuations. It should be noted that no thresholding is applied, and the conditional correlation only depends on the sign of streamwise and spanwise velocity fluctuations. It is identical to the conditional two-point correlation used by Sillero *et al.* (2014) and de Silva *et al.* (2018). The conditional correlation is defined as

$$R^{CPW}_{u_2u_2} = \frac{\langle u_2(x_2, x_3)u_2(x_2 + \Delta x_2, x_3 + \Delta x_3)\rangle \,|\, u_3 > 0}{\sigma^2_{u_2} \,|\, u_3 > 0}, \tag{3.4}$$

for positive spanwise velocity fluctuations and

$$R^{CNW}_{u_2u_2} = \frac{\langle u_2(x_2, x_3)u_2(x_2 + \Delta x_2, x_3 + \Delta x_3)\rangle \,|\, u_3 < 0}{\sigma^2_{u_2} \,|\, u_3 < 0}, \tag{3.5}$$

for negative spanwise velocity fluctuations.

The streamwise–spanwise two-point correlations of streamwise velocity fluctuations conditioned on the signs of streamwise and spanwise velocity fluctuations are shown in figures 12 and 13. The high-speed and low-speed streamwise velocity correlations exhibit

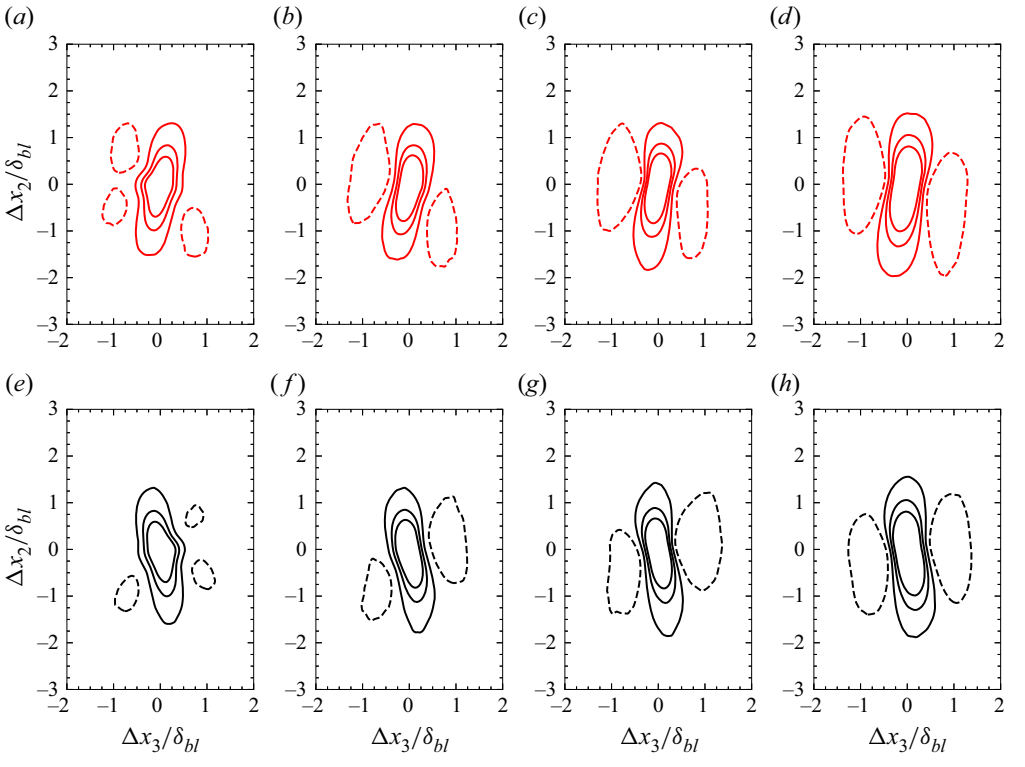

Figure 12. Streamwise–spanwise two-point conditional correlation coefficient $R^{CPW}_{u_2u_2}$ of fast-moving structures at (*a*,*e*) $x_1/\delta_{bl} = 0.04$ (*b*,*f*) $x_1/\delta_{bl} = 0.1$, (*c*,*g*) $x_1/\delta_{bl} = 0.3$ and (d,h) $x_1/\delta_{bl} = 0.6$. Red contours in (*a–d*) represent $R^{CPW}_{u_2u_2}$ of positive u_3 and black contours in (*e–h*) represent $R^{CPW}_{u_2u_2}$ of negative u_3. The contour lines are -0.05, 0.05, 0.15 and 0.25. Negative values are represented using dashed contours.

spanwise drift in the inner and outer layers. This statistical signature is similar to what is observed by de Silva *et al.* (2018) in the logarithmic region of the turbulent boundary layer, implying that the meandering of the LSMs in the turbulent buoyancy layer is related to spanwise velocity fluctuations.

In terms of the correlations presented here, spanwise velocity fluctuations affect both high-speed and low-speed LSMs equally. The orientation of the two-point conditional correlation coefficients is similar across the thickness of the boundary layer, implying that the meandering due to spanwise velocity fluctuations is consistent. However, this does not indicate that the interaction mechanisms are the same. For fast-moving streamwise velocity fluctuations (shown in figure 12), positive spanwise velocity fluctuations induce a positive spanwise drift (oriented to the right in the streamwise direction of the flow). In contrast, negative spanwise velocity fluctuations cause a negative spanwise drift (oriented to the left in the streamwise direction of the flow). The opposite is the case for the slow-moving velocity fluctuations (shown in figure 13). Positive spanwise velocity fluctuations induce a negative spanwise drift, and negative spanwise velocity fluctuations cause a positive spanwise drift in low-speed LSMs. This suggests that positive and negative spanwise velocity fluctuations interact differently with high-speed and low-speed motions.

For the given thresholding of spanwise velocities fluctuations, it is interesting to note that the spanwise drift of the LSMs is more significant in the turbulent buoyancy layer than the turbulent boundary layer. In turbulent boundary layers, solely in terms of

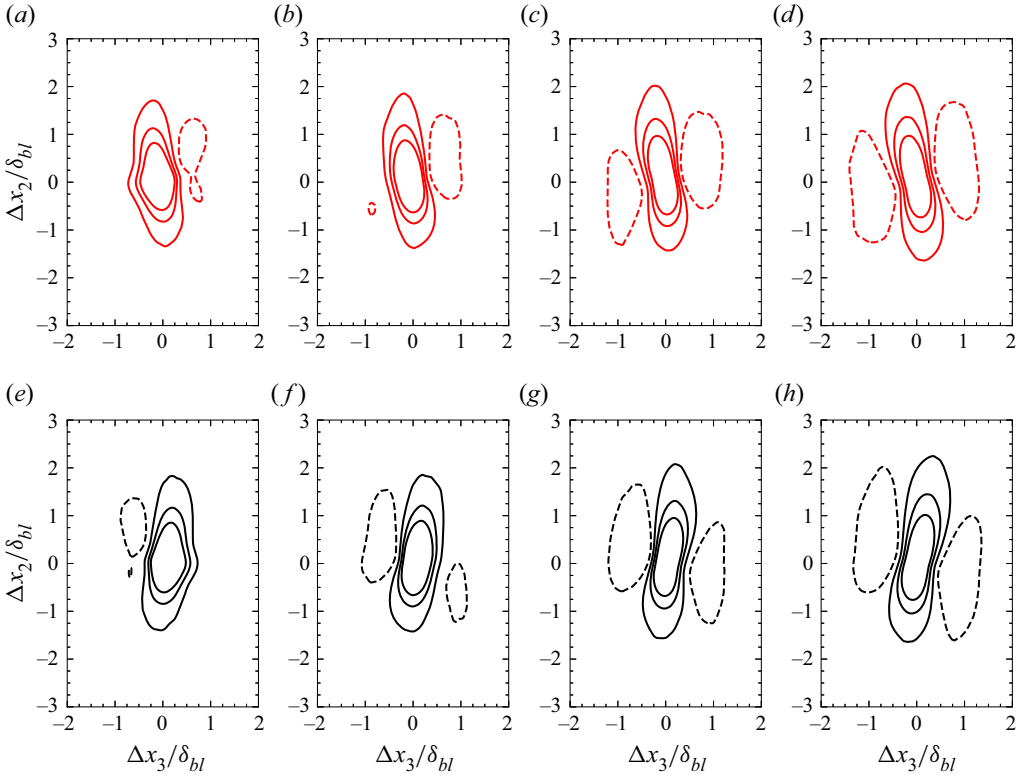

Figure 13. Streamwise–spanwise two-point conditional correlation coefficient $R^{CNW}_{u_2u_2}$ of slow-moving structures at (*a*,*e*) $x_1/\delta_{bl} = 0.04$ (*b*,*f*) $x_1/\delta_{bl} = 0.1$, (*c*,*g*) $x_1/\delta_{bl} = 0.3$ and (*d*,*h*) $x_1/\delta_{bl} = 0.6$. Red contours (*a–d*) represent $R^{CNW}_{u_2u_2}$ of positive u_3 and black contours (*e–h*) represent $R^{CNW}_{u_2u_2}$ of negative u_3. The contour lines are −0.05, 0.05, 0.15 and 0.25. Negative values are represented using dashed contours.

two-point correlations, for the given threshold, the spanwise drift is significant at the edge of the boundary layer. It is only marginal in the logarithmic layer (de Silva *et al.* 2018). In the present case, a high degree of preferential orientation of the two-point conditional streamwise correlations is observed at all the four wall-normal locations shown in figures 12 and 13. This suggests that the spanwise velocity fluctuations in the turbulent buoyancy layer can induce a more significant spanwise drift to the LSMs than the turbulent boundary layer.

3.2.3. *Wall-normal coherence*

The two-point correlations above reveal LSMs' streamwise and spanwise coherence in the turbulent buoyancy layer. In this section, the two-point wall-normal correlation is calculated to investigate the streamwise velocity fluctuations' wall-normal coherence. The two-point wall-normal correlation is calculated using

$$R^{W}_{u_2u_2} = \frac{\langle u_2(x_{1ref}, x_2) u_2(x_1, x_2 + \Delta x_2)\rangle}{\sigma_{u_2(x_{1ref})}\sigma_{u_2(x_1)}}, \tag{3.6}$$

where $\sigma_{u_2(x_{1ref})}$ is the standard deviation at a reference wall-normal location and $\sigma_{u_2(x_1)}$ is the standard deviation at a wall-normal location x_1.

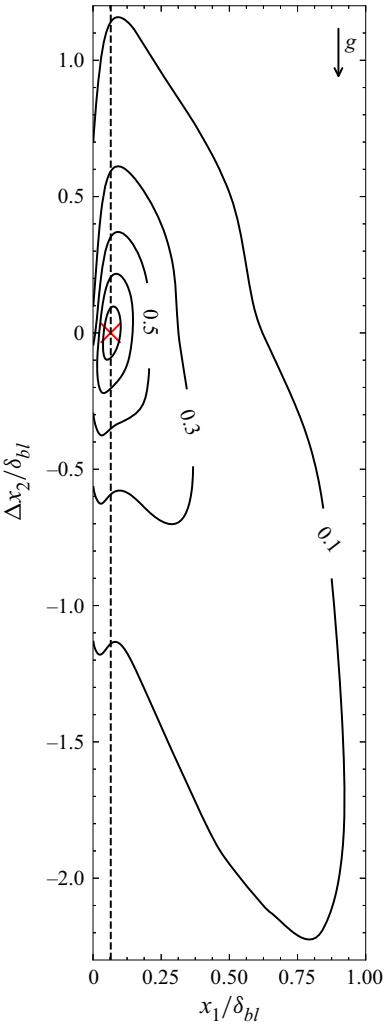

Figure 14. Wall-normal–streamwise two-point correlation coefficient ($R^W_{u_2u_2}$) map of streamwise velocity fluctuations. The black contour lines are equally spaced from 0.1 to 0.9. The red cross represents the reference location, and the black dashed line separates the inner and outer layers. Gravity ($\boldsymbol{g}$) acts in the negative x_2 direction (downwards), and the fluid flows in the positive x_2 direction (upwards).

Figure 14 shows the statistically averaged structure arising from the two-point wall-normal correlation of the streamwise velocity fluctuations. The reference height is chosen as $x_1 = 0.065\delta_{bl}$, which is the wall-normal location where the mean streamwise velocity is maximum. This also corresponds to the location in the boundary layer where the mean shear is zero.

It is evident from the figure that the streamwise velocity fluctuations exhibit coherence over significant wall-normal distances. The positive two-point correlation coefficient contours are present for almost the entire boundary layer thickness. Large-scale coherence is also present in the downstream and upstream directions, along with substantial wall-normal correlation. This implies that, statistically, large-scale structures are responsible for turbulence in the turbulent buoyancy layer. It should be noted that the presence of non-zero values for two-point correlations across significant wall-normal

distances is also observed in unstratified turbulent NCBLs (Tsuji *et al.* 1992; Abedin *et al.* 2012; Nakao *et al.* 2017).

The differences in the shape of the statistical structure shown in figure 14 and the wall-normal statistical structure of canonical wall-bounded turbulence are immediately evident. In canonical wall-bounded turbulence, a ramp-like structure inclined in the downstream direction of the flow is observed, which is believed to be the consequence of a packet of hairpin-like vortex structures (Christensen & Adrian 2001; Ganapathisubramani *et al.* 2005; Adrian 2007; Marusic & Adrian 2012; Baltzer *et al.* 2013; Hwang *et al.* 2016). In the turbulent buoyancy layer, a ramp-like structure inclined in the downstream direction is observed in the inner layer. In contrast, the ramp-like structure is inclined in the upstream direction in the outer layer. The differences between the wall-normal coherence of the LSMs in the turbulent buoyancy layer and canonical wall-bounded turbulence can be attributed to the presence of different vortex structures due to the change in the sign of the mean shear in the outer layer (Nakao *et al.* 2017). At this stage, the role of hairpin vortices or similar in NCBL transition and turbulence is not fully understood (Pallares *et al.* 2010; Abramov *et al.* 2014; Nakao *et al.* 2017; Zhao *et al.* 2017, 2019) and no definitive conclusions can be drawn that relate hairpin-like vortex structures observed in prior studies to the two-point correlations discussed in this study.

To quantify the tilt of the two-point correlation shown in figure 14, the structure inclination angle (Carper & Porté-Agel 2004; Marusic & Heuer 2007; Chauhan *et al.* 2013; Deshpande, Monty & Marusic 2019) is calculated using the velocity maximum as the reference position. It is calculated as

$$\theta = \arctan(x_1^*/\Delta s), \tag{3.7}$$

where θ is the structural inclination angle, x_1^* is the absolute wall-normal separation distance between the velocity maximum and the location of interest, and Δs is the streamwise spatial separation corresponding to the peak of correlation $R^W_{u_2u_2}$. Note that Δs can take both positive and negative values, with positive values indicating a spatial separation in the downstream direction and negative values indicating a spatial separation in the upstream direction.

Figure 15 shows the structure inclination angle at different wall-normal locations in the turbulent buoyancy layer. A single dominant inclination angle is absent, agreeing with figure 14. In the inner layer, θ is positive and is around 24°. In the outer layer, θ is approx. 55° at small separation distances and decays to approx. −25° with increasing wall-normal distance. Here, positive values of θ indicate that Δs is positive and that the structure is inclined in the downstream direction. On the other hand, negative values of θ indicate that Δs is negative and that the structure is inclined in the upstream direction.

The structures responsible for the large-scale wall-normal coherence are also visible in the instantaneous flow fields. Figure 16 shows the instantaneous streamwise velocity field across the mid-span of the domain at three different times (the exact time instant is irrelevant as the flow fields represent developed turbulence that is statistically homogeneous in the streamwise (x_2) and spanwise (x_3) directions). It is clear from the figure that the large-scale flow structures spanning almost the entire boundary layer thickness populate the buoyancy layer. This is reminiscent of the large-scale eddies observed in unstratified vertical NCBLs (Fujii 1959; Vliet & Liu 1969; Tsuji & Nagano 1988*b*; Hattori *et al.* 2006; Abedin *et al.* 2017), highlighting the qualitative similarities between the two flows. Close to the wall ($x_1 \lessapprox 0.2$), the velocity flow structures are inclined in the downstream direction, while away from the wall ($x_1 \gtrapprox 0.2$), the flow structures are tilted in the upstream direction, agreeing with the two-point correlation and structure inclination angle plots in figures 14 and 15, respectively.

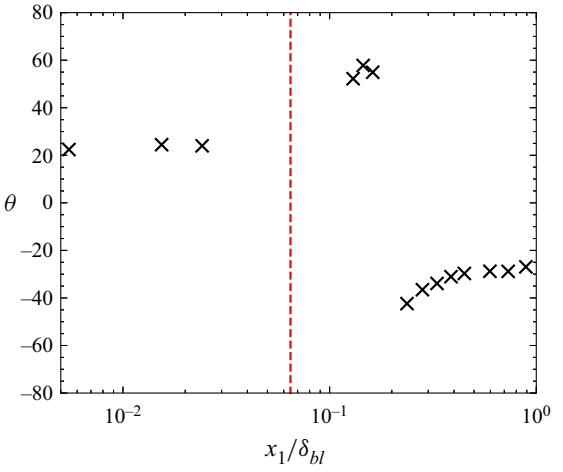

Figure 15. Variation of structure inclination angle θ with respect to the wall-normal location. The red dashed line indicates the reference position, which is also the location of the velocity maximum.

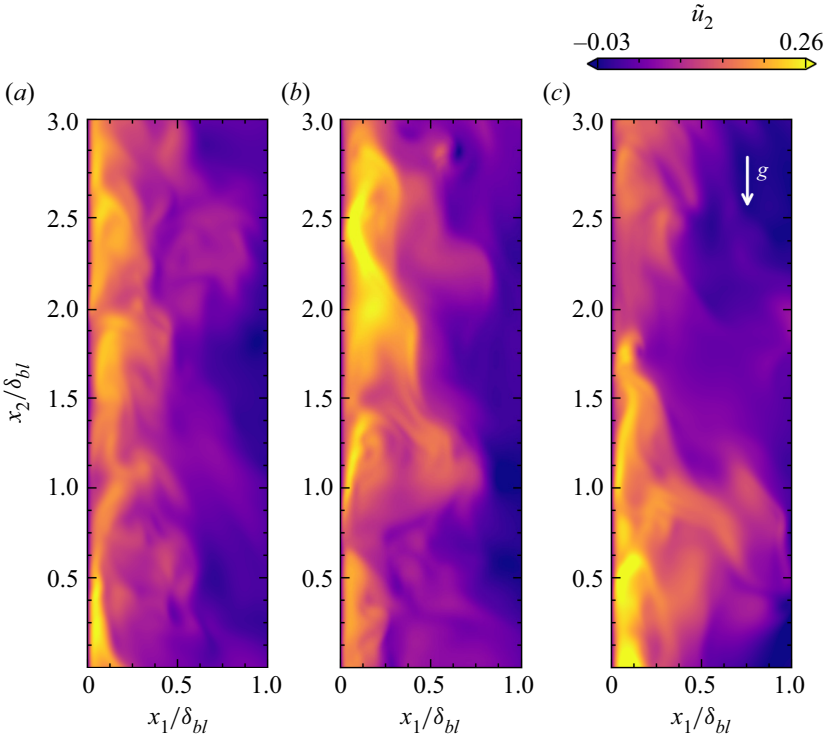

Figure 16. Three different snapshots of the instantaneous streamwise velocity ($\tilde{u}_2$) field at the mid-span of the domain. Gravity ($\boldsymbol{g}$) acts in the negative x_2 direction, and the fluid flows in the positive x_2 direction. Only a portion of the entire domain is shown.

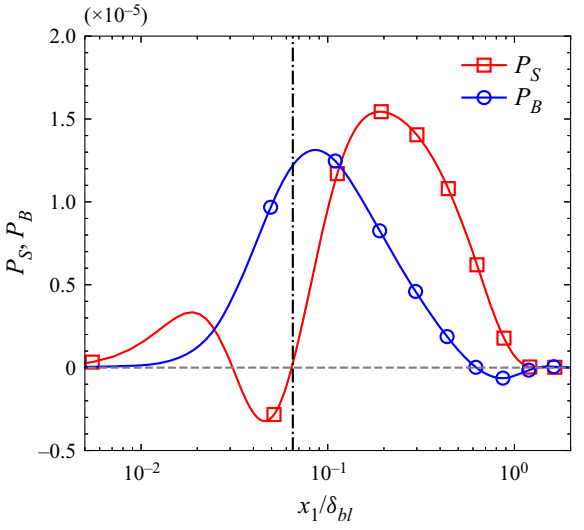

Figure 17. Wall-normal variation of the production of TKE due to shear (P_S) and buoyancy (P_B). The black dot-dashed vertical line represents the wall-normal location of the velocity maximum, which is used to demarcate the inner and the outer layers.

3.2.4. *Role of LSMs in turbulence production*

In turbulent buoyancy layers, the Reynolds shear stress and the streamwise turbulent heat flux are responsible for the production of TKE (Giometto *et al.* 2017; Maryada *et al.* 2022). The shear production (P_S) and buoyancy flux (P_B) are defined as

$$P_S = -\langle u_1 u_2 \rangle \frac{\partial \overline{u_2}}{\partial x_1}, \tag{3.8a}$$

$$P_B = \frac{2}{Re} \langle u_1 \vartheta \rangle. \tag{3.8b}$$

The wall-normal variation of the shear production and the buoyancy flux are shown in figure 17. It is clear from the figure that both shear and buoyancy are dominant producers of TKE in the vertical buoyancy layer. Most of the TKE is produced in the outer layer at the Prandtl number and Reynolds number investigated, consistent with the DNS results of Giometto *et al.* (2017). It should be noted that despite the flow being driven by buoyancy, shear still dominates over buoyancy in terms of TKE production. The relative dominance of shear over buoyancy was also observed in unstratified NCBLs and transitional buoyancy layers having a Prandtl number of 0.71 (Janssen & Armfield 1996; Maryada *et al.* 2022). Similarities between the current flow at $Pr = 0.71$ and the flow at $Pr = 1$ (Giometto *et al.* 2017) are also immediately evident, where shear dominates TKE production. This is in contrast to transitional unstratified vertical NCBLs at $Pr = 7.0$ where buoyancy dominates (Zhao *et al.* 2017).

In the inner layer, the shear production is positive in a layer close to the wall. In a region that is bounded by this layer and the velocity maximum, the shear production is negative. It indicates counter-gradient turbulent flux, a characteristic feature of turbulent buoyancy layers (Giometto *et al.* 2017). In this region, the buoyancy flux is positive and is responsible for most of the production of TKE. In the outer layer, P_S mostly dominates over P_B until the edge of the boundary layer. Near the edge of the boundary layer, at $x_1 > 0.6\delta_{bl}$, P_B is negative, suggesting that buoyancy at these wall-normal locations is responsible for the

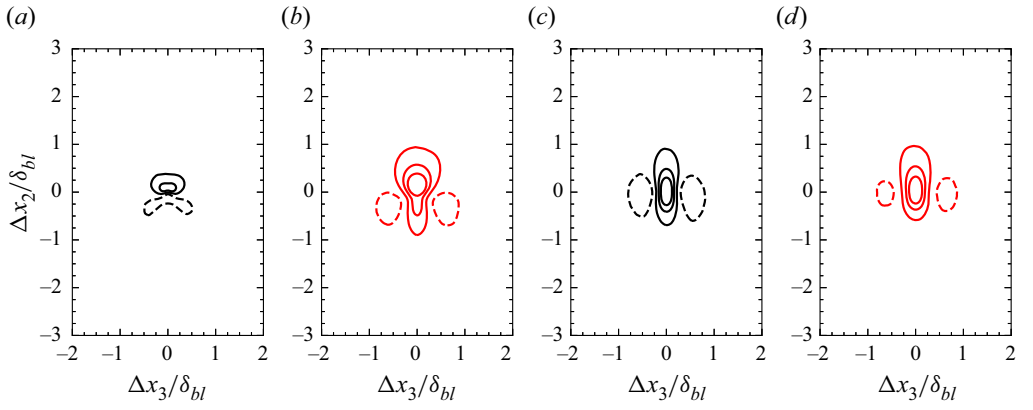

Figure 18. Streamwise–spanwise two-point cross-conditional correlation coefficient map of Reynolds shear stress $R^{CC}_{u_1u_2}$ and streamwise turbulent heat flux $R^{CC}_{u_2\vartheta}$ at (*a*,*b*) $x_1/\delta_{bl} = 0.04$ and (*c*,*d*) $x_1/\delta_{bl} = 0.3$. Black contours in (*a*,*c*) represents $R^{CC}_{u_1u_2}$ and red contours in (*b*,*d*) represents $R^{CC}_{u_2\vartheta}$. The contour lines are −0.05, 0.05, 0.15 and 0.25. Negative values are represented using dashed contours.

destruction of TKE. The dual role of buoyancy flux in producing and destroying TKE was also observed in transitional buoyancy layers (Maryada *et al.* 2022).

Figure 17 only indicates the wall-normal locations where the TKE production is dominant. The two-point cross-correlations of u_1 and u_2 ($R^{CC}_{u_1u_2}$), and u_2 and ϑ ($R^{CC}_{u_2\vartheta}$) are calculated to understand the momentum and heat transfer associated with the LSMs. These are defined as

$$R^{CC}_{u_1u_2} = \frac{\langle u_1(x_2, x_3)u_2(x_2 + \Delta x_2, x_3 + \Delta x_3)\rangle}{\sigma_{u_1}\sigma_{u_2}}, \tag{3.9a}$$

$$R^{CC}_{u_2\vartheta} = \frac{\langle u_2(x_2, x_3)\vartheta(x_2 + \Delta x_2, x_3 + \Delta x_3)\rangle}{\sigma_{u_2}\sigma_{\vartheta}}. \tag{3.9b}$$

The two-point cross-correlations of Reynolds shear stress and streamwise turbulent heat flux at $x_1 = 0.04\delta_{bl}$ and $x_1 = 0.3\delta_{bl}$ are shown in figure 18. The wall-normal location of $x_1 = 0.04\delta_{bl}$ represents the wall-normal location in the inner layer where the buoyancy variance is significant. In comparison, $x_1 = 0.3\delta_{bl}$ represents the wall-normal location in the outer layer where the wall-normal velocity variance and Reynolds shear stress are significant (see figure 4).

It is evident from figure 18(*a*) that, in the inner layer, the two-point cross-correlation of the Reynolds shear stress does not extend to large streamwise and spanwise distances, implying the absence of large-scale coherence. This suggests that the high-speed or low-speed LSMs are not strongly correlated with the wall-normal velocity fluctuations.

In figure 18(*c*), large-scale coherence of Reynolds shear stress is observed in the outer layer, albeit with a shorter length scale than streamwise velocity fluctuations (see figure 9). The two-point cross-correlation of Reynolds shear stress in a turbulent boundary layer also has a shorter streamwise length scale than the streamwise length scale of the two-point correlation of streamwise velocity fluctuations (Sillero *et al.* 2014).

The two-point correlation map in figure 18(*c*) shows a region of positive correlation flanked by regions of negative correlation. This implies that the high-speed streamwise velocity fluctuations are correlated with positive wall-normal velocity fluctuations, and the low-speed streamwise velocity fluctuations are correlated with negative wall-normal

velocity fluctuations. Therefore, the high-speed fluid in the outer layer comprises an upwash flow, while the low-speed fluid in the outer layer comprises a downwash flow.

The mean Reynolds shear stress is negative in the inner layer and positive in the outer layer of the vertical buoyancy layer (see figure 4*b*), and the positive value of the cross-correlation near $\Delta x_2 = \Delta x_3 = 0$ is consistent with the sign of the Reynolds shear stress in the outer layer.

If a decomposition of the Reynolds shear stress is made according to quadrant analysis (Wallace 2016), it would imply that the high-speed LSMs are composed of $Q1$ quadrant events ($u_1 > 0, u_2 > 0$) and the low-speed LSMs are composed of $Q3$ quadrant events ($u_1 < 0, u_2 < 0$). It should be stressed that this is opposite to what is observed in canonical wall-bounded turbulence, where $Q2$ ($u_1 < 0, u_2 > 0$) and $Q4$ ($u_1 > 0, u_2 < 0$) events dominate the flow field (Ganapathisubramani *et al.* 2005; Dennis & Nickels 2011; Lee & Sung 2011; Hwang *et al.* 2016; Wallace 2016).

Large-scale streamwise coherence is observed in the two-point cross-correlation maps of streamwise turbulent heat flux in both the inner and outer layers, evident in figure 18(*b*,*d*). The streamwise length scale of the streamwise turbulent heat flux is shorter than the streamwise length scale of streamwise velocity fluctuations. Similar to the two-point correlation of the Reynolds shear stress, $R^{CC}_{u_2\vartheta}$ is biased in the downstream direction.

Regions of negative streamwise two-point cross-correlation surround a region of positive two-point correlation. This indicates that the positive streamwise velocity fluctuations are correlated with positive buoyancy perturbations (higher temperature than the mean buoyancy field). Negative streamwise velocity fluctuations are correlated with negative buoyancy perturbations (lower temperature than the mean buoyancy field). Decomposing the streamwise turbulent heat flux using quadrant analysis would imply that the high-speed motions are composed of $Q1$ quadrant events ($u_1 > 0, \vartheta > 0$) and the low-speed LSMs comprised $Q3$ quadrant events ($u_1 < 0, \vartheta < 0$).

The positive value of the cross-correlation near $\Delta x_2 = \Delta x_3 = 0$ is consistent with the ensembled averaged streamwise turbulent heat flux, which is positive across most of the turbulent buoyancy layer and is only negative at its edge (see figure 4*b*).

By comparing the cross-correlations of the Reynolds shear stress and streamwise turbulent heat flux, it is clear that the high-speed LSMs are composed of upwash flow having relatively higher temperatures, and the low-speed LSMs are composed of downwash flow having relatively lower temperatures.

To better understand this distribution of Reynolds shear stress and streamwise turbulent heat flux, the instantaneous streamwise velocity fluctuations overlayed with intense events of Reynolds shear stress and streamwise turbulent heat flux are shown in figure 19. The visualisation is similar to the one used by Dennis & Nickels (2011), who investigated LSMs in a turbulent boundary layer. In the inner layer, the intense events of Reynolds shear stress and streamwise turbulent heat flux are marginally better correlated with low-speed motions (figure 19*a*,*c*), suggesting that low-speed motions are the dominant contributors of Reynolds shear stress and turbulent heat flux. High-speed motions also contribute to Reynolds shear stress and streamwise turbulent heat flux but do not carry significant portions of them. The distribution of Reynolds shear stress is similar to that of Reynolds shear stress in turbulent boundary layers (Dennis & Nickels 2011).

The distribution of Reynolds shear stress and streamwise turbulent heat flux in the outer layer (figure 19*b*,*d*) reveals the striking differences between the turbulent buoyancy layer and canonical wall-bounded turbulence. In the outer layer, the extreme events of the Reynolds shear stress and the streamwise turbulent heat flux are strongly correlated

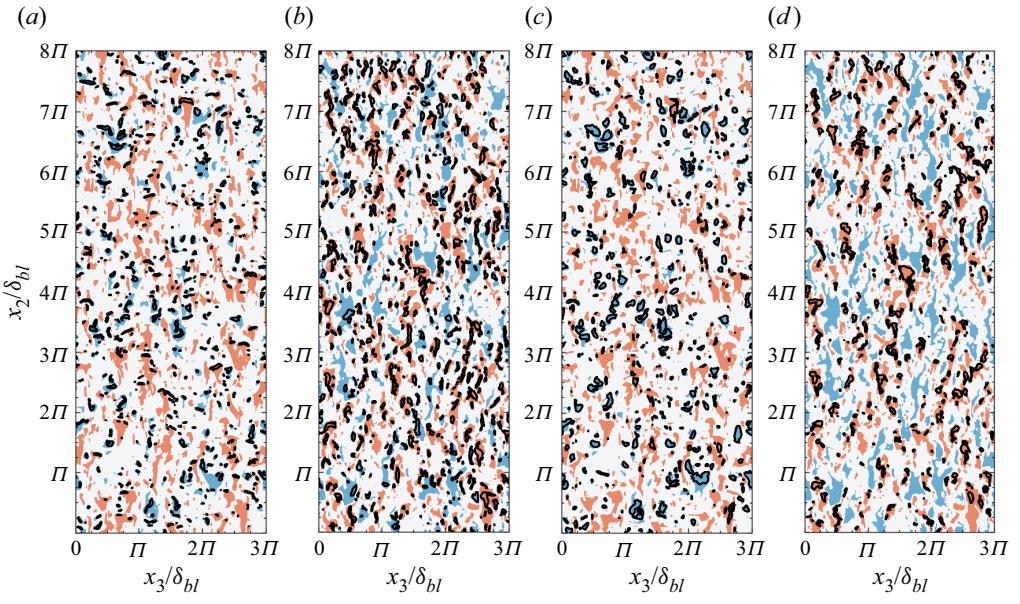

Figure 19. Instantaneous intense positive (red) and negative (blue) streamwise velocity fluctuations overlayed with contours (black) of intense events of Reynolds shear stress and streamwise turbulent heat flux at (*a*,*c*) $x_1/\delta_{bl} = 0.04$ and (*b*,*d*) $x_1/\delta_{bl} = 0.3$. The red contours correspond to $u_2 > 0.25\overline{u_{2m}}$ and the blue contours correspond to $u_2 < -0.25\overline{u_{2m}}$ where $\overline{u_{2m}}$ is the maximum mean flow velocity. The black contour lines in (*a*,*b*) correspond to the contours of $\langle u_1 u_2 \rangle > 2\sigma_{\langle u_1 u_2 \rangle}$ and the black contour lines in (*c*,*d*) correspond to the contours of $\langle u_2 \vartheta \rangle > 2\sigma_{\langle u_1 \vartheta \rangle}$, where σ is the standard deviation. Gravity acts in the negative x_2 direction, and the fluid flows in the positive x_2 direction.

with high-speed LSMs, implying that the high-speed LSMs are the dominant contributors of Reynolds shear stress and streamwise turbulent heat flux in the outer layer. This differs from canonical wall-bounded turbulence where low-speed LSMs are shown to be dynamically more important (Dennis & Nickels 2011). Quadrant analysis (Wallace 2016) also demonstrates that the $Q1$ events ($u_1, u_2 > 0$ and $u_2, \vartheta > 0$) contribute around 60 % of mean Reynolds shear stress and around 65 % of mean streamwise turbulent heat flux at $x_1 = 0.3\delta_{bl}$. As the high-speed LSMs mostly comprised $Q1$ events, it can be presumed that the high-speed LSMs are responsible for most of the production of TKE in the outer layer. This is qualitatively similar to unstratified turbulent NCBLs, where $Q1$ events in the outer layer significantly contribute to Reynolds shear stress (Hattori *et al.* 2006).

3.3. *Streamwise and spanwise energy spectra*

Along with two-point correlations, premultiplied spectra can indicate the presence of large-scale structures in turbulent flows (Toh & Itano 2005; Hutchins & Marusic 2007). The premultiplied one-dimensional streamwise and spanwise spectra of u_2^+ are shown in figure 20. The premultiplied spectra demonstrate that most of the streamwise energy is present in the outer layer of the turbulent buoyancy layer at the Reynolds number investigated. Only a minimal amount of streamwise energy is present in the inner layer. This is consistent with the mean values reported in figure 4(*a*), which is expected as the integral of the energy spectra of streamwise velocity fluctuations is equivalent to the ensemble-averaged streamwise velocity variance.

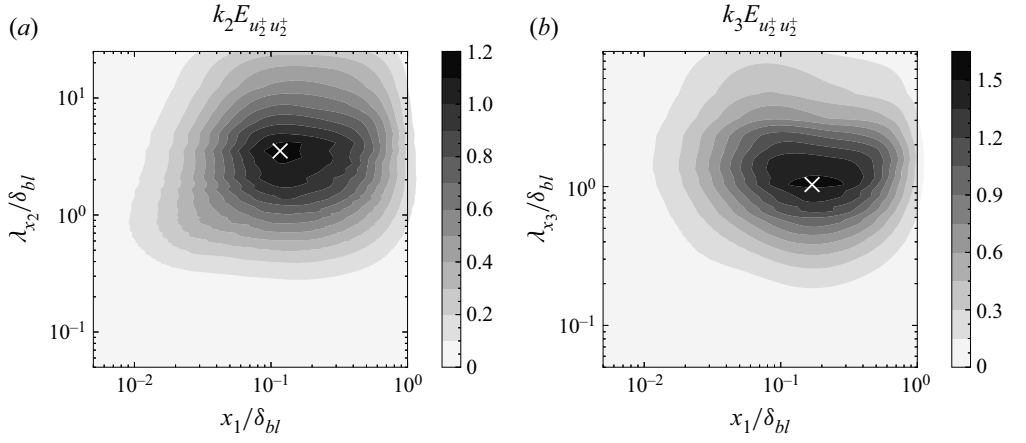

Figure 20. Premultiplied one-dimensional energy spectra of u_2^+. (*a*) Spectra in the streamwise direction and (*b*) spectra in the spanwise direction. The horizontal and vertical axes are normalised by the boundary layer thickness. White crosses are used to indicate the location of the peak of the energy spectra.

The premultiplied streamwise energy spectrum shown in figure 20(*a*) exhibits an energy peak at $x_1 \approx 0.12\delta_{bl}$ and $\lambda_{x_2} \approx 3.5\delta_{bl}$ (shown with a white cross in figure 20*a*). The premultiplied spanwise energy spectrum shown in figure 20(*b*) has an energy peak at $x_1 \approx 0.17\delta_{bl}$ and $\lambda_{x_3} \approx \delta_{bl}$ (shown with a white cross in figure 20*b*). Here, λ_{x_2} and λ_{x_3} are the streamwise and spanwise wavelengths, respectively. At $x_1 \approx 0.17\delta_{bl}$, in the streamwise direction, the dominant wavelength is similar to the streamwise length scale of 3 obtained from the two-point streamwise correlations. At $x_1 \approx 0.17\delta_{bl}$, in the spanwise direction, the wavelength corresponding to the energy peak is similar to the spanwise length of 0.75 obtained from the two-point streamwise correlations. Minor differences are expected as the length scales are calculated using a finite threshold for the two-point correlation coefficient (Sillero *et al.* 2014). Nevertheless, this suggests that the dominant energy-containing motions in the turbulent buoyancy layer are located in the outer layer at the Reynolds number investigated and are related to LSMs of streamwise velocity fluctuations.

Even in terms of one-dimensional streamwise and spanwise energy spectra of streamwise velocity fluctuations, the characteristics of the LSMs observed in the present case are different from what is traditionally observed in turbulent boundary layers. In the zero pressure gradient turbulent boundary layer, a spectral peak is observed close to the wall whose wavelength scales well with viscous units, not the outer ones. It is commonly referred to as the inner peak and is a consequence of the quasi-streamwise vortices in the inner wall cycle (Hutchins & Marusic 2007; Jiménez 2018). An outer peak in the spectra is observed only at high Re_τ (Hutchins & Marusic 2007; Marusic 2001; Smits *et al.* 2011; Marusic & Adrian 2012; Solak & Laval 2018). The turbulent vertical buoyancy layer exhibits dominant signatures of energetic large-scale structures at this Re_τ, evident from figure 20. This suggests that moderate-Re_τ is sufficient to observe LSMs in turbulent vertical buoyancy layers. Therefore, it is stressed that despite Re_τ being used to quantify the turbulent character of the vertical buoyancy layer, a direct comparison with the zero pressure gradient turbulent boundary layer at the same Re_τ to examine LSMs should be avoided.

From figure 20, it is also evident that the streamwise and spanwise domain extents are large enough to enclose the most energetic contours of streamwise velocity perturbations, validating the choice of the domain size.

4. Conclusions

Using two-point correlations and one-dimensional streamwise and spanwise energy spectra, it has been demonstrated that streamwise velocity fluctuations in the turbulent buoyancy layer having a Prandtl number of 0.71 at a Reynolds number of 800 exhibit large-scale streamwise coherence. The large-scale streamwise coherence is due to LSMs having streamwise length scales greater than the boundary layer thickness. Such large-scale streamwise coherence is notably absent in wall-normal and spanwise velocity fluctuations and buoyancy fluctuations.

Both the positive (high-speed) and negative (low-speed) streamwise velocity perturbations form long and narrow LSMs in the inner and outer layers. The two-point correlations show that the low-speed LSMs exhibit streamwise coherence over larger distances than the high-speed LSMs; however, this difference is only marginal. The LSMs, especially in the outer layer, meander significantly, and this meandering is correlated with the sign of the spanwise velocity fluctuations. The meandering due to spanwise velocity fluctuations is dominant across most of the outer layer of the vertical buoyancy layer.

Two-point correlation in the wall-normal direction demonstrates that the LSMs extend across almost the entire thickness of the boundary layer, indicating significant wall-normal coherence. In the inner layer, the statistical structure is inclined in the downstream direction; however, in the outer layer, the structure is inclined in the upstream direction.

In the outer layer, two-point correlations and conditional sampling reveal that the high-speed LSMs are related to upwash flow having relatively higher temperatures, and the low-speed LSMs are related to downwash flow having relatively lower temperatures. The high-speed LSMs are dynamically more relevant in producing turbulence kinetic energy than the low-speed LSMs.

Comparing the two-point correlations and premultiplied streamwise and spanwise energy spectra shows that the streamwise velocity motions exhibiting large-scale coherence are the dominant energy-containing motions in the turbulent buoyancy layer, implying that at the Reynolds number investigated, the length scale of energy-containing eddies is of the order of the boundary layer thickness.

Overall, it is demonstrated that large-scale high-speed and low-speed motions populate the turbulent buoyancy layer and are dynamically relevant for producing and sustaining turbulence.

Acknowledgements. We thank New Zealand eScience Infrastructure (NeSI) for providing high performance computing facilities.

Funding. This research received no specific grant from any funding agency, commercial or not-for-profit sectors.

Declaration of interests. The authors report no conflict of interest.

Author ORCIDs.
K.R. Maryada https://orcid.org/0000-0003-3509-0176;
S.W. Armfield https://orcid.org/0000-0002-8032-0017;
P. Dhopade https://orcid.org/0000-0003-2011-9300;
S.E. Norris https://orcid.org/0000-0001-5255-8741.

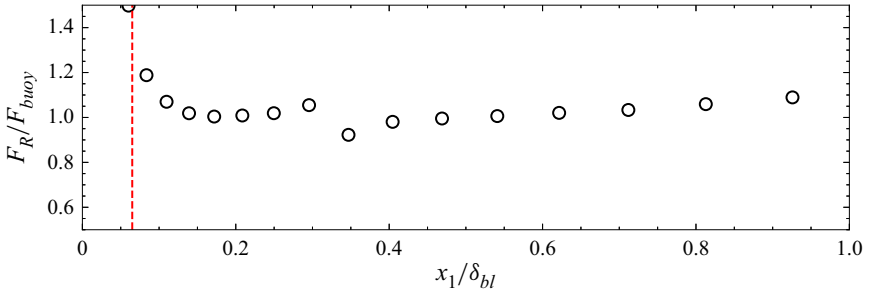

Figure 21. The ratio of the gradient of the Reynolds stress F_R to the buoyancy force F_{buoy}. The red dashed vertical line represents the location of the velocity maximum, demarcating the inner layer from the outer layer.

Appendix A. Viscous effects in the outer layer of the buoyancy layer

For a fully developed turbulent boundary layer, the Navier–Stokes equation in (2.2*a*), with the help of Reynolds decomposition, can be simplified as

$$\underbrace{\frac{\partial \langle u_1 u_2 \rangle}{\partial x_1}}_{F_R} = \underbrace{\frac{1}{Re}\frac{\partial^2 \overline{u_2}}{\partial x_1^2}}_{F_{visc}} + \underbrace{\frac{2}{Re}\bar{\vartheta}}_{F_{buoy}}, \tag{A1}$$

where F_R is the gradient of the Reynolds shear stress or the turbulent force, F_{visc} is the viscous force, and F_{buoy} is the force due to buoyancy.

The above equation states that, throughout the buoyancy layer, there is a balance between the viscous force, the gradient of the Reynolds shear stress and buoyancy. This does not imply that all the terms are equal at all the wall-normal locations. Different terms are dominant at different wall-normal locations of the buoyancy layer. This force balance is qualitatively similar to that observed in canonical wall-bounded turbulence (Fife *et al.* 2005; Wei *et al.* 2005).

In a high-Re_τ wall-bounded turbulent flow, viscous effects are expected to dominate in regions close to the wall, and they are no longer the leading-order terms in regions far away from the wall. Then, the force balance equation in (A1) can be simplified to

$$\underbrace{\frac{\partial \langle u_1 u_2 \rangle}{\partial x_1}}_{F_R} \approx \underbrace{\frac{2}{Re}\bar{\vartheta}}_{F_{buoy}}, \tag{A2}$$

such that there is a balance between the gradient of the Reynolds shear stress and buoyancy. It should be noted that no specific assumptions are made regarding the magnitude of Re_τ except that the flow is representative of a fully developed turbulent flow. A similar analysis was carried out in unstratified vertical natural convection (Wei 2020; Wei, Wang & Abraham 2021).

If the Re_τ investigated in the current study is representative of such a fully developed flow, then the balance in (A2) is also expected to hold. Figure 21 shows the ratio of the buoyancy force to the gradient of the Reynolds shear stress. It is evident from the figure that the gradient of the Reynolds shear stress is in approximate balance with buoyancy for most of the outer layer, demonstrating that the viscous effects are not significant. As viscous force is not dominant in the outer layer, ν is not a controlling parameter of the flow (Wei 2020; Wei *et al.* 2021). This demonstrates that, despite viscosity being dominant close to the wall, its impact is negligible away from the wall, with it only acting on

small-scale eddies. Similar conclusions regarding the effect of viscosity were also drawn in canonical wall-bounded turbulence (Fife *et al.* 2005; Wei *et al.* 2005; Marusic *et al.* 2013). This suggests that the low-Re effects are expected to be only marginal in the outer layer at $Re = 800$.

References

Abedin, M.Z., Tsuji, T. & Hattori, Y. 2009 Direct numerical simulation for a time-developing natural-convection boundary layer along a vertical flat plate. *Intl J. Heat Mass Transfer* **52** (19-20), 4525–4534.

Abedin, M.Z., Tsuji, T. & Kim, N.H. 2017 Higher-order and length-scale statistics of velocity and temperature fluctuations in turbulent boundary layer along a heated vertical flat plate. *Intl J. Heat Fluid Flow* **65**, 252–265.

Abedin, M.Z., Tsuji, T. & Lee, J. 2012 Turbulence characteristics and vortical structures in combined-convection boundary layers along a heated vertical flat plate. *Intl J. Heat Mass Transfer* **55** (15-16), 3995–4002.

Abramov, A.G., Smirnov, E.M. & Goryachev, V.D. 2014 Temporal direct numerical simulation of transitional natural-convection boundary layer under conditions of considerable external turbulence effects. *Fluid Dyn. Res.* **46** (4), 041408.

Adrian, R.J. 2007 Hairpin vortex organization in wall turbulence. *Phys. Fluids* **19** (4), 041301.

Armfield, S. & Street, R. 2002 An analysis and comparison of the time accuracy of fractional-step methods for the Navier–Stokes equations on staggered grids. *Intl J. Numer. Meth. Fluids* **38** (3), 255–282.

Armfield, S.W. 1994 Ellipticity, accuracy, and convergence of the discrete Navier–Stokes equations. *J. Comput. Phys.* **114** (2), 176–184.

Armfield, S.W., Morgan, P., Norris, S. & Street, R. 2003 A parallel non-staggered Navier–Stokes solver implemented on a workstation cluster. In *Computational Fluid Dynamics 2002* (ed. S.W. Armfield, P. Morgan & K. Srinivas), pp. 30–45. Springer.

Bae, H.J. & Lee, M. 2021 Life cycle of streaks in the buffer layer of wall-bounded turbulence. *Phys. Rev. Fluids* **6** (6), 064603.

Baltzer, J.R., Adrian, R.J. & Wu, X. 2013 Structural organization of large and very large scales in turbulent pipe flow simulation. *J. Fluid Mech.* **720**, 236–279.

Bejan, A. 2013 *Convection Heat Transfer*, 4th edn. John Wiley & Sons.

Carper, M.A. & Porté-Agel, F. 2004 The role of coherent structures in subfilter-scale dissipation of turbulence measured in the atmospheric surface layer. *J. Turbul.* **5** (1), 040.

Chauhan, K., Hutchins, N., Monty, J. & Marusic, I. 2013 Structure inclination angles in the convective atmospheric surface layer. *Boundary-Layer Meteorol.* **147**, 41–50.

Cheesewright, R. 1968 Turbulent natural convection from a vertical plane surface. *J. Heat Transfer* **90** (1), 1–6.

Cheesewright, R. & Doan, K.S. 1978 Space-time correlation measurements in a turbulent natural convection boundary layer. *Intl J. Heat Mass Transfer* **21** (7), 911–921.

Christensen, K.T. & Adrian, R.J. 2001 Statistical evidence of hairpin vortex packets in wall turbulence. *J. Fluid Mech.* **431**, 433–443.

Dennis, D.J.C. & Nickels, T.B. 2011 Experimental measurement of large-scale three-dimensional structures in a turbulent boundary layer. Part 2. Long structures. *J. Fluid Mech.* **673**, 218–244.

Deshpande, R., Monty, J.P. & Marusic, I. 2019 Streamwise inclination angle of large wall-attached structures in turbulent boundary layers. *J. Fluid Mech.* **877**, R4.

Eckert, E.R.G. & Jackson, T.W. 1950 Analysis of turbulent free-convection boundary layer on flat plate. Tech. Memorandum NACA-TN-2207. National Advisory Committee for Aeronautics.

Fan, Y., Zhao, Y., Torres, J.F., Xu, F., Lei, C., Li, Y. & Carmeliet, J. 2021 Natural convection over vertical and horizontal heated flat surfaces: a review of recent progress focusing on underpinnings and implications for heat transfer and environmental applications. *Phys. Fluids* **33** (10), 101301.

Fedorovich, E. & Shapiro, A. 2009*a* Structure of numerically simulated katabatic and anabatic flows along steep slopes. *Acta Geophys.* **57** (4), 981–1010.

Fedorovich, E. & Shapiro, A. 2009*b* Turbulent natural convection along a vertical plate immersed in a stably stratified fluid. *J. Fluid Mech.* **636**, 41–57.

Fife, P., Wei, T., Klewicki, J. & McMurtry, P. 2005 Stress gradient balance layers and scale hierarchies in wall-bounded turbulent flows. *J. Fluid Mech.* **532**, 165–189.

FUJII, T. 1959 On the development of a vortex street in a free convection boundary layer. *Bull. JSME* **2** (8), 551–555.

GANAPATHISUBRAMANI, B., HUTCHINS, N., HAMBLETON, W.T., LONGMIRE, E.K. & MARUSIC, I. 2005 Investigation of large-scale coherence in a turbulent boundary layer using two-point correlations. *J. Fluid Mech.* **524**, 57–80.

GEBHART, B. 1973 Instability, transition, and turbulence in buoyancy-induced flows. *Annu. Rev. Fluid Mech.* **5** (1), 213–246.

GILL, A.E. 1966 The boundary-layer regime for convection in a rectangular cavity. *J. Fluid Mech.* **26** (3), 515–536.

GILL, A.E. & DAVEY, A. 1969 Instabilities of a buoyancy-driven system. *J. Fluid Mech.* **35** (4), 775–798.

GIOMETTO, M.G., KATUL, G.G., FANG, J. & PARLANGE, M.B. 2017 Direct numerical simulation of turbulent slope flows up to Grashof number $Gr = 2.1 \times 10^{11}$. *J. Fluid Mech.* **829**, 589–620.

HATTORI, Y., TSUJI, T., NAGANO, Y. & TANAKA, N. 2006 Turbulence characteristics of natural-convection boundary layer in air along a vertical plate heated at high temperatures. *Intl J. Heat Fluid Flow* **27** (3), 445–455.

HUTCHINS, N., HAMBLETON, W.T. & MARUSIC, I. 2005 Inclined cross-stream stereo particle image velocimetry measurements in turbulent boundary layers. *J. Fluid Mech.* **541**, 21–54.

HUTCHINS, N. & MARUSIC, I. 2007 Evidence of very long meandering features in the logarithmic region of turbulent boundary layers. *J. Fluid Mech.* **579**, 1–28.

HWANG, J., LEE, J., SUNG, H.J. & ZAKI, T.A. 2016 Inner–outer interactions of large-scale structures in turbulent channel flow. *J. Fluid Mech.* **790**, 128–157.

JALURIA, Y. & GEBHART, B. 1974 On transition mechanisms in vertical natural convection flow. *J. Fluid Mech.* **66** (2), 309–337.

JANSSEN, R. & ARMFIELD, S.W. 1996 Stability properties of the vertical boundary layers in differentially heated cavities. *Intl J. Heat Fluid Flow* **17** (6), 547–556.

JIMÉNEZ, J. 2018 Coherent structures in wall-bounded turbulence. *J. Fluid Mech.* **842**, P1.

KE, J., WILLIAMSON, N., ARMFIELD, S.W., KOMIYA, A. & NORRIS, S.E. 2021 High Grashof number turbulent natural convection on an infinite vertical wall. *J. Fluid Mech.* **929**, A15.

KE, J., WILLIAMSON, N., ARMFIELD, S.W., NORRIS, S.E. & KOMIYA, A. 2020 Law of the wall for a temporally evolving vertical natural convection boundary layer. *J. Fluid Mech.* **902**, A31.

KEVIN, K., MONTY, J. & HUTCHINS, N. 2019 The meandering behaviour of large-scale structures in turbulent boundary layers. *J. Fluid Mech.* **865**, R1.

KIM, K.C. & ADRIAN, R.J. 1999 Very large-scale motion in the outer layer. *Phys. Fluids* **11** (2), 417–422.

KIM, K.H., AHN, J. & CHOI, J.I. 2021 Mean thermal energy balance analysis in differentially heated vertical channel flows. *Phys. Fluids* **33** (6), 065120.

KITAMURA, K., KOIKE, M., FUKUOKA, I. & SAITO, T. 1985 Large eddy structure and heat transfer of turbulent natural convection along a vertical flat plate. *Intl J. Heat Mass Transfer* **28** (4), 837–850.

KOZUL, M., CHUNG, D. & MONTY, J.P. 2016 Direct numerical simulation of the incompressible temporally developing turbulent boundary layer. *J. Fluid Mech.* **796**, 437–472.

LEE, J., AHN, J. & SUNG, H.J. 2015 Comparison of large-and very-large-scale motions in turbulent pipe and channel flows. *Phys. Fluids* **27** (2), 025101.

LEE, J., LEE, J.H., CHOI, J.I. & SUNG, H.J. 2014 Spatial organization of large-and very-large-scale motions in a turbulent channel flow. *J. Fluid Mech.* **749**, 818–840.

LEE, J.H. 2017 Large-scale motions in turbulent boundary layers subjected to adverse pressure gradients. *J. Fluid Mech.* **810**, 323–361.

LEE, J.H. & SUNG, H.J. 2011 Very-large-scale motions in a turbulent boundary layer. *J. Fluid Mech.* **673**, 80–120.

LEE, J.H. & SUNG, H.J. 2013 Comparison of very-large-scale motions of turbulent pipe and boundary layer simulations. *Phys. Fluids* **25** (4), 045103.

LILLY, D.K. 1965 On the computational stability of numerical solutions of time-dependent non-linear geophysical fluid dynamics problems. *Mont. Weath. Rev.* **93** (1), 11–25.

LOCHET, R., LEMONNIER, D. & DOAN-KIM-SON, 1983 Correlations en convection naturelle turbulente. Influence de la pression et de la nature du gaz. *Intl J. Heat Mass Transfer* **26** (8), 1221–1227.

LOCK, G.S.H. & TROTTER, F.J.D. 1968 Observations on the structure of a turbulent free convection boundary layer. *Intl J. Heat Mass Transfer* **11** (8), 1225–1232.

MARUSIC, I. 2001 On the role of large-scale structures in wall turbulence. *Phys. Fluids* **13** (3), 735–743.

MARUSIC, I. & ADRIAN, R. 2012 The eddies and scales of wall turbulence. In *Ten Chapters in Turbulence* (ed. P.A. Davidson, Y. Kaneda & K.R. Sreenivasan), pp. 176–220. Cambridge University Press.

MARUSIC, I. & HEUER, W.D.C. 2007 Reynolds number invariance of the structure inclination angle in wall turbulence. *Phys. Rev. Lett.* **99** (11), 114504.

MARUSIC, I., MONTY, J.P., HULTMARK, M. & SMITS, A.J. 2013 On the logarithmic region in wall turbulence. *J. Fluid Mech.* **716**, R3.

MARYADA, K.R., ARMFIELD, S.W., DHOPADE, P. & NORRIS, S.E. 2022 Oblique-mode breakdown of the vertical buoyancy layer. *J. Fluid Mech.* **953**, A34.

MCBAIN, G.D., ARMFIELD, S.W. & DESRAYAUD, G. 2007 Instability of the buoyancy layer on an evenly heated vertical wall. *J. Fluid Mech.* **587**, 453–469.

MOIN, P. & KIM, J. 1982 Numerical investigation of turbulent channel flow. *J. Fluid Mech.* **118**, 341–377.

MONTY, J.P., HARUN, Z. & MARUSIC, I. 2011 A parametric study of adverse pressure gradient turbulent boundary layers. *Intl J. Heat Fluid Flow* **32** (3), 575–585.

MONTY, J.P., STEWART, J.A., WILLIAMS, R.C. & CHONG, M.S. 2007 Large-scale features in turbulent pipe and channel flows. *J. Fluid Mech.* **589**, 147–156.

NAKAO, K., HATTORI, Y. & SUTO, H. 2017 Numerical investigation of a spatially developing turbulent natural convection boundary layer along a vertical heated plate. *Intl J. Heat Fluid Flow* **63**, 128–138.

NG, C.S., OOI, A., LOHSE, D. & CHUNG, D. 2017 Changes in the boundary-layer structure at the edge of the ultimate regime in vertical natural convection. *J. Fluid Mech.* **825**, 550–572.

NORRIS, S.E. 2000 A parallel Navier–Stokes solver for natural convection and free surface flow. PhD thesis, The University of Sydney, Camperdown, NSW.

PALLARES, J., VERNET, A., FERRE, J.A. & GRAU, F.X. 2010 Turbulent large-scale structures in natural convection vertical channel flow. *Intl J. Heat Mass Transfer* **53** (19-20), 4168–4175.

PRANDTL, L. 1952 *Essentials of Fluid Dynamics*. Blackie & Son.

RHIE, C.M. & CHOW, W.L. 1983 Numerical study of the turbulent flow past an airfoil with trailing edge separation. *AIAA J.* **21** (11), 1525–1532.

ROBINSON, S.K. 1991 Coherent motions in the turbulent boundary layer. *Annu. Rev. Fluid Mech.* **23** (1), 601–639.

SAAD, Y. & SCHULTZ, M.H. 1986 GMRES: a generalized minimal residual algorithm for solving nonsymmetric linear systems. *SIAM J. Sci. Stat. Comput.* **7** (3), 856–869.

SCHLATTER, P. & ÖRLÜ, R. 2010 Assessment of direct numerical simulation data of turbulent boundary layers. *J. Fluid Mech.* **659**, 116–126.

SCHUMANN, U. 1990 Large-eddy simulation of the up-slope boundary layer. *Q. J. R. Meteorol. Soc.* **116** (493), 637–670.

SILLERO, J.A., JIMÉNEZ, J. & MOSER, R.D. 2014 Two-point statistics for turbulent boundary layers and channels at Reynolds numbers up to $\delta^+ \approx 2000$. *Phys. Fluids* **26** (10), 105109.

DE SILVA, C.M., KEVIN, K., BAIDYA, R., HUTCHINS, N. & MARUSIC, I. 2018 Large coherence of spanwise velocity in turbulent boundary layers. *J. Fluid Mech.* **847**, 161–185.

SMITS, A.J., MCKEON, B.J. & MARUSIC, I. 2011 High-Reynolds number wall turbulence. *Annu. Rev. Fluid Mech.* **43** (1), 353–375.

SOLAK, I. & LAVAL, J.P. 2018 Large-scale motions from a direct numerical simulation of a turbulent boundary layer. *Phys. Rev.* E **98** (3), 033101.

STONE, H.L. 1968 Iterative solution of implicit approximations of multidimensional partial differential equations. *SIAM J. Numer. Anal.* **5** (3), 530–558.

TOH, S. & ITANO, T. 2005 Interaction between a large-scale structure and near-wall structures in channel flow. *J. Fluid Mech.* **524**, 249–262.

TSUJI, T. & NAGANO, Y. 1988*a* Characteristics of a turbulent natural convection boundary layer along a vertical flat plate. *Intl J. Heat Mass Transfer* **31** (8), 1723–1734.

TSUJI, T. & NAGANO, Y. 1988*b* Turbulence measurements in a natural convection boundary layer along a vertical flat plate. *Intl J. Heat Mass Transfer* **31** (10), 2101–2111.

TSUJI, T., NAGANO, Y. & TAGAWA, M. 1992 Experiment on spatio-temporal turbulent structures of a natural convection boundary layer. *J. Heat Transfer* **114** (4), 901–908.

VERSTEEGH, T.A.M. & NIEUWSTADT, F.T.M. 1998 Turbulent budgets of natural convection in an infinite, differentially heated, vertical channel. *Intl J. Heat Fluid Flow* **19** (2), 135–149.

VLIET, G.C. & LIU, C.K. 1969 An experimental study of turbulent natural convection boundary layers. *J. Heat Transfer* **91** (4), 517–531.

VAN DER VORST, H.A. 1992 Bi-CGSTAB: a fast and smoothly converging variant of Bi-CG for the solution of nonsymmetric linear systems. *SIAM J. Sci. Stat. Comput.* **13** (2), 631–644.

WALLACE, J.M. 2016 Quadrant analysis in turbulence research: history and evolution. *Annu. Rev. Fluid Mech.* **48**, 131–158.

WEI, T. 2020 Analyses of buoyancy-driven convection. In *Advances in Heat Transfer* (ed. J.P. Abraham, J.M. Gorman & W.J. Minkowycz), vol. 52, pp. 1–93. Elsevier.

WEI, T., FIFE, P., KLEWICKI, J. & MCMURTRY, P. 2005 Properties of the mean momentum balance in turbulent boundary layer, pipe and channel flows. *J. Fluid Mech.* **522**, 303–327.

WEI, T., WANG, Y. & ABRAHAM, J. 2021 Layered structure of turbulent natural convection over a vertical flat plate. *Intl J. Heat Mass Transfer* **181**, 121866.

ZHAO, Y., LEI, C. & PATTERSON, J.C. 2016 Natural transition in natural convection boundary layers. *Intl Commun. Heat Mass Transfer* **76**, 366–375.

ZHAO, Y., LEI, C. & PATTERSON, J.C. 2017 The K-type and H-type transitions of natural convection boundary layers. *J. Fluid Mech.* **824**, 352–387.

ZHAO, Y., LEI, C. & PATTERSON, J.C. 2019 PIV measurements of the K-type transition in natural convection boundary layers. *J. Expl Therm. Fluid Sci.* **101**, 62–75.